

In-situ TEM studies of 150 keV W⁺ ion irradiated W and W-alloys: Damage production and microstructural evolution

Xiaoou Yi ^{a,b,*}, Michael L Jenkins ^c, Marquis A Kirk ^d, Zhongfu Zhou ^{e,f} and Steven G Roberts ^{a,b}

^a Department of Materials, University of Oxford, Parks Road, Oxford, OX1 3PH, U.K.

^b CCFE, Culham Science Centre, Abingdon, OX14 3DB, U.K.

^c Trinity College, University of Oxford, Broad Street, Oxford, OX1 3BH, U.K.

^d Nuclear Engineering Division, Argonne National Laboratory, Argonne, IL 60439, U.S.A.

^e Key Laboratory for Material Microstructures, Shanghai University, Shanghai 200444, China.

^f Institute of Mathematics and Physics, Aberystwyth University, Aberystwyth, SY23 3BZ, U.K.

*Corresponding author: xiaoou.yi@materials.ox.ac.uk

Abstract

In-situ irradiations with 150 keV W⁺ ions have been performed on W and W-5wt.% (Re; Ta; V) alloys in a comprehensive study of the influences of irradiation temperature T_{irr}, dose, alloying elements and grain orientations on radiation damage production and microstructural evolution. For T_{irr} between 30 K and 1073 K, the first observable defects in pure W appeared at doses ≤ 0.01 dpa, and were most likely vacancy loops, with Burgers vectors predominantly of type **b** = ½ <111>. With increasing T_{irr}, the retained defect concentration decreased strongly and the maximum cluster size increased from ~ 1300 point defects at 30 K to ~ 2300 point defects at 1073 K. At all irradiation temperatures, the evolution of damage microstructures with dose from 0.1 to 1.0 dpa involved defect cluster migration, with mutual elastic interactions often leading to spatial inhomogeneities and loop reactions. In pure W, spatial ordering of loops was observed at doses > 0.4 dpa and T_{irr} ≥ 773 K in grains close to **z** = <001>. No such ordering was found in similar grain orientations for the W-(Re; Ta) alloys, but it was found in the non-**z** = <001> grains. Post-irradiation analysis on W and W-5 wt% (Re; Ta) at 1.0 dpa showed that ½ <111> and <100> loops of both vacancy and interstitial type were present, at number densities ~ 10¹⁵ loops m⁻². In all cases ½ <111> loops were dominant, the fraction of these with interstitial nature increased with T_{irr}, and the proportion of <100> loops decreased with increasing T_{irr}. Compared with pure W, microstructures in the W-(Re; Ta) alloys exhibited higher loop number densities and evolved more quickly with increasing dose towards damage saturation.

Keywords: W/W-alloys; In-situ irradiations; TEM; Damage production; Microstructure evolution.

1. Introduction

Tungsten is a prime candidate for building divertor (“exhaust”) components in fusion reactors. These components will run at temperatures 1250-1600 K and the high incident flux of fusion neutrons may generate up to 30 - 40 dpa of displacement damage per year [1]. Transmutation reactions from the fusion neutrons also alter the composition: under reactor conditions, pure tungsten produces percentage quantities of rhenium, osmium, and tantalum after a few years of operation [2]. The synergistic effects of displacement damage, transmutation and the deposition of He “ash” (the product of D-T fusion reactions) may lead to hardening, reduced fracture toughness, and to a loss of dimensional stability due to swelling and creep [3]. These are serious challenges for the application of tungsten in fusion applications and they call for an in-depth understanding of the mechanisms responsible for the nucleation and evolution of radiation damage, along with the development of modelling tools for the reliable prediction of material performance during the lifetime of the reactor.

Early-stage damage in tungsten was studied in the 1970s and 80s by *in-situ* field ion microscopy (FIM). Wei et al [4, 5] and Current et al. [6] investigated the populations, sizes and spatial correlation of vacancies (singly, in small clusters or larger depleted zones) and self-interstitial atoms (SIAs) in single-crystal W tips of ~ 25 nm average initial radius. The effects of irradiations with 15 - 70 keV single-ion beams (W^+ , Cr^+ , Ar^+ etc), up to a dose of $\sim 5 \times 10^{16}$ ions m^{-2} (i.e. no cascade overlap [4, 5]) were investigated at $T_{irr} \leq 15$ K, to eliminate the thermal migration of point defects, as confirmed in [7]. Three notable trends were reported: 1) heavier ions produced more compact cascades; 2) a power-law type scaling was found for the distribution of sizes of vacancy clusters; 3) the total number of vacancies was found to be an order of magnitude higher than the number of SIAs, implying a significant effect of the presence of nearby free surfaces.

Studies of early-stage damage development in W have also been made by diffraction-contrast imaging in transmission electron microscopy (TEM), which has a typical spatial resolution limit of ~ 1.5 nm. The larger volumes examinable by TEM give information complementary to that from FIM, in particular allowing the imaging of dislocation loops which originate from the collapse of large vacancy-rich regions (typically containing 30 vacancies or more [8]), and giving better statistical information on the densities and types of defects. Most of the observed loops were glissile and could easily be lost to a free surface, which would render them unobservable in FIM tips.

Häussermann, Wilkens, Rühle and Jäger irradiated thin foils of W at 300 K with 20-70 keV Au^+ ions to doses $\leq 5 \times 10^{15}$ ions m^{-2} [9-12]. Only about 10% of 60 keV Au^+ ion impacts resulted in the formation of a visible loop, with an average diameter of 2.77 nm [11]. The visible defects were identified as vacancy loops, predominantly of pure-edge type with Burgers vectors $\mathbf{b} = \frac{1}{2} \langle 111 \rangle$, together with a small number of faulted loops with $\mathbf{b} = \frac{1}{2} \langle 110 \rangle$. No loops with $\mathbf{b} = \langle 100 \rangle$ were reported. Recent work of Yi et al. [13] extended the irradiation temperature range to 773 K, with 150 keV W^+ ion irradiations to a constant dose of $\sim 10^{16}$ ions m^{-2} . Visible defect yields were as low as ~ 1 % and the average loop size was ~ 3.45 nm. Both $\frac{1}{2} \langle 111 \rangle$ and $\langle 100 \rangle$ loops were identified [14, 15], and all were likely to be of vacancy type. No evidence of faulted loops was found. Both early and recent results on radiation damage evolution in pure W are in good agreement with the predictions of the Eyre-Bullough mechanism, whereby loops in bcc metals nucleate as faulted loops on $\{110\}$ planes before unfaulting to prismatic loops [12, 16].

These experimental studies of early-stage damage have been complemented by molecular dynamics (MD) simulations of displacement cascades in bulk material, FIM tips and thin foils. A pronounced influence of the surface on damage evolution was found [17]. In addition, the sizes of clusters of both vacancies and of SIAs were found to follow a power-

law scaling with their frequency of occurrence, up to a primary knock-on energy of 200 keV. The threshold energy for sub-cascade formation was estimated slightly above 150 keV [18, 19]. Loops with Burgers vectors of type $\frac{1}{2} \langle 111 \rangle$ and $\langle 100 \rangle$ loops and of both interstitial and of vacancy nature were found to co-exist [20]. However, in these models, most clusters were produced near surfaces and which would be large enough to be resolvable by TEM (i.e. with point defect number, $N > 30$) were of vacancy type [20], in good agreement with the experiments [8, 13]. Despite this promising progress, MD simulations, which are limited to ~ 50 ion impacts on a time scale < 1 ns, do not yet offer a comparable level of statistics to FIM or TEM experiments (10^3 - 10^4 ion impacts; 10-100s). This gap has been bridged by object Kinetic Monte Carlo (okMC) simulations. The recent work of Mason et al. [8] not only quantitatively captured the temperature dependence of damage evolution in W found in the experiments [8, 13], but also identified the dominant role of elastic trapping among defect clusters.

Damage evolution in W at cascade-overlap doses has been examined to a lesser extent and much of the understanding has come from indirect electrical resistivity measurements. Five distinct ranges of temperature were defined for fast neutron damage in W [21, 22], based on the dominant mechanism controlling defect evolution: 20 - 100 K (Stage I), recombination of Frenkel pairs and the migration of free SIAs; 100 - 700 K (Stage II), detrapping of SIAs from dislocations and impurity atoms; 700 - 920 K (Stage III), vacancy migration; 920 - 1270 K (Stage IV), migration of vacancy clusters and vacancy-impurity complexes; 1270 - 1800 K (Stage V), thermal dissociation of vacancy and /or interstitial clusters. However, an in-depth understanding of damage evolution requires additional experimental data on the roles of irradiation temperature, dose, dose rate and grain orientation in determining defect cluster types, defect morphologies, defect populations, size distributions and spatial correlations.

Hasegawa and co-workers [23, 24] pioneered such detailed studies in pure W, irradiated by fission neutron irradiations (0.09 - 1.54 dpa, 700 - 1100 K). In the low-dose (< 0.5 dpa) and low-temperature ($T \leq 800$ K) regime, the visible defect species were mostly voids as well as small numbers of loops. In the high-dose (≥ 0.5 dpa) and high-temperature ($T > 800$ K) regime, void growth was favoured and void lattice structures were observed at a dose of ~ 1 dpa. These authors further postulated that at ~ 10 dpa, when the transmuted Re increases to a few wt%, void lattices would lose stability, concomitant with the nucleation and coarsening of precipitates (σ -phase: ReW; χ -phase: Re₃W) [23, 25].

Ion irradiations as a proxy for fast neutrons allow some convenience and better control of irradiation parameters. Ciupiński et al. [26] and Yi et al. [27] have used self-ion irradiation to study trends with dose (0.01 - 30 dpa) and irradiation temperature (300 - 1023 K) for $\langle 001 \rangle$ -grains¹ [28] of W and W-alloys, utilising cross-sectional and planar specimen geometries respectively. Both sets of authors confirmed that in Stage II, loops with $\mathbf{b} = \frac{1}{2} \langle 111 \rangle$ ($\sim 75\%$) and $\mathbf{b} = \langle 100 \rangle$ coexist, and were mostly ≤ 6 nm in diameter and interstitial in nature [22]. These loops coarsened with increasing dose. For 2 MeV W⁺ ions, uniform distributions of loops were maintained up to 30 dpa [27]; while for 20 MeV W⁶⁺ ions, ordered damage structures emerged at 0.1 dpa [26]. During Stage III, loops from 2 MeV W⁺ irradiations exhibited further coarsening and up to $\sim 95\%$ were identified as $\frac{1}{2} \langle 111 \rangle$ loops of interstitial nature [22]. These loops rearranged to strings (also termed chains²) at ≥ 1.2 dpa. Finally in Stage IV [22], the overall fraction of $\frac{1}{2} \langle 111 \rangle$ interstitial loops was close to unity, along with

¹ Grain orientation was not specified in the Ciupiński paper. However, judging from the heat treatment condition (2470 K, 10 min), the samples must have been fully recrystallized and exhibiting the $\{001\} \langle 100 \rangle$ cube texture.

² Chains consist of resolved loops. In strings individual loops are not resolved. The basic morphology is the same.

an increased degree of ordering to strings. The presence of 5% Re and Ta resulted in consistently higher loop populations and strongly inhibited the evolution of damage microstructures.

Post-irradiation examination of near-bulk irradiations (i.e. ones where free surface effects on the evolution of radiation damage are largely suppressed) enable quantitative correlation of irradiation parameters with features of damage microstructures. However, information on the real-time-evolution of damage is not available from such experiments. This requires the use of irradiation facilities with *in-situ* recording/imaging capability. Previous experimental work in such facilities has been reported for iron [29-36] and molybdenum [37], and has been coordinated with modelling using MD, cluster dynamics and Langevin dynamics [38-41]. These studies have shown that the dynamic behaviour of defect clusters - especially loop migration, mutual interaction and reactions - are largely responsible for changes in the sizes, populations, geometries and spatial distribution of the damage microstructure. Similar *in-situ* radiation damage studies on W and W-5Re have been performed by Yi et al. [13], but that investigation was restricted to a single irradiation temperature of 773 K.

In this paper, we report results on a wide range of materials and irradiation parameters, continuing the use of 150 keV W^+ ions as a surrogate of the average primary recoil particles from fusion neutrons [42]. The irradiations cover a temperature range of 30 - 1073 K and a dose range of 0.01 - 1.0 dpa, over a collection of W and W- (Re, Ta, V) alloys. Dynamic defect behaviour, size distributions, populations, geometries, nature and spatial distributions are characterized, in correlation with the roles of irradiation parameters (temperature, dose), alloying elements and grain orientations, so as to investigate the mechanisms involved in damage nucleation and microstructural evolution. We conclude with a brief comparison between thin-foil irradiations (150 keV W^+ ions) and near-bulk irradiations (~ 2 MeV W^+ ions) so as to distinguish effects that are intrinsic to the material itself from those that result from the effects of surface tractions.

2. Experimental details

Polycrystalline pure W and W-5 wt.% Re (hot rolled, ~ 150 μm sheets) and W-5 wt.% (Ta; V) alloys (hot forged ingots) were sourced from Plansee Gruppe, Austria. Typical impurity levels (mostly C, O, Fe, Mo) were no more than 40 ppm for pure W and 300 ppm for W-5 wt.% (Re; Ta; V) alloys [43]. 3 mm discs were cut from the as-received materials, mechanically thinned to around 80 μm , annealed in vacuum at 1673 K for 20 hours and electropolished. Details of polishing recipes for pure W, W-5(Re; Ta) have been described in [27]. The recipe used for W-5V was the same as for pure W.

In-situ irradiations were carried out on the IVEM-Tandem facility at Argonne National Laboratory (ANL) [33]. A beam of 150 keV W^+ ions³ was directed to a Hitachi H-9000NAR TEM operating at 300 kV. The irradiation conditions covered a wide range of temperatures from 30 K to 1073 K and a dose range from 10^{16} to 10^{18} W^+ m^{-2} at a constant rate of $\sim 6.25 \times 10^{14}$ W^+ $m^{-2}s^{-1}$ and are summarised in Table 1. A Gatan Orius 1000 camera recorded still micrographs and the defect dynamics at 15 frames s^{-1} . A double-tilt heating stage was used to allow favourable imaging conditions for diffraction contrast. The sample temperature was measured to within ± 5 K using Cr-Al thermocouple wires attached to the Ta-furnace. A high angle of incidence of the ion beam ($\sim 75^\circ$) was maintained by tilting the specimen stage $\sim 15^\circ$ towards the ion beam. For the experiments at 30 K, a double-tilt liquid helium cooling

³ The ion beam was weakly focused and apertured to a diameter of 1.5 mm. This was effectively the beam spot size on the sample. Further slight rastering of the beam was applied for a smooth and flattened beam profile.

stage was used. Details of the damage profile calculation with SRIM 2008 have been described in [13], where the dose range corresponds to 0.01-1.0 dpa and peaks at ~15 nm beneath the irradiated surface. Note that some results of the low-dose (~ 0.01 dpa) experiments on pure W have been published in a joint paper of modelling and experiments [8], although without detailed contrast analysis of loops.

Recovery experiments were performed on pure W samples only, irradiated to 1.0 dpa at 300 K and then annealed at 573 K, 773 K and 1073 K for up to 2 hours. The study reported here focuses on the effects of temperature upon defect migration (section 3.4.1). Further detailed investigations of damage annealing in tungsten have been published in [44, 45].

Post-irradiation examination was performed on $\mathbf{z} = \langle 001 \rangle$ oriented grains of pure W and W-5 wt.% (Re; Ta) alloys⁴ [46, 47] using a Hitachi TEM (ANL) and a Philips CM20 (Oxford). Foil thickness measurements with electron energy loss spectroscopy (EELS) were performed on a JEM 3000F (Oxford). Note that in W-5V nearly all grains had normals close to $\mathbf{z} = \langle 011 \rangle$ and the material was therefore used only for defect dynamic behaviour studies (section 3.4.2).

3. Results

3.1. Damage production in pure W at low doses (up to 0.01 dpa)

Early-stage damage production in pure W was studied over an irradiation temperature range of 30 - 1073 K. Two imaging modes were applied for the TEM characterization of damage production: a weak-beam dark-field (WBDF) condition ($\mathbf{z} = \langle 001 \rangle$, $\mathbf{g} = \pm 200/020$, $3\text{-}4\mathbf{g}$) for measurements of loop number densities and sizes throughout the irradiations; and a strong dynamical condition for the determination by black-white (B-W) contrast of defect geometry (loop Burgers vectors and habit planes) and interstitial/vacancy nature at the conclusion of the irradiation. The dose limit of 0.01 dpa was chosen in order to avoid overlap of cascades [13], and this is validated by plots of defect population against irradiation dose (Fig. 1), where the slopes k of the log-log plots are all close to unity; at a given irradiation temperature, the areal number density is therefore proportional to irradiation dose, consistent with an intra-cascade process where the probability for the production and survival of a visible loop within an individual cascade in a thin-foil of a given material depends on temperature, PKA energy, the position of the cascade within the foil and the foil orientation, but not on the dose or dose-rate [48].

Loop nucleation and development within individual cascades in pure W was dependent on the irradiation temperature. At $T_{\text{irr}} \leq 873$ K, dislocation loops appeared suddenly from one frame to the next within 0.07s of the start of the irradiation and no further measurable loop growth or change in image contrast was observed. At 1073 K however, loop formation was not seen until ~ 1s after the start of the irradiation. The image contrast again appeared abruptly but increased in brightness and size over a period of ~ 0.3s, and then remained stable for the remainder of the experiment. The microstructures at the end of the experiment at the different irradiation temperatures are shown in Fig. 2. With an increase of T_{irr} from 300 K to 1073 K, the rate of loop accumulation dropped by a factor of ~ 6.5 (Fig. 1)⁵ but average loop sizes increased (Fig. 2).

⁴ Heat-treated pure W and W-5Re samples exhibited strong textures of $\{001\}\langle 110 \rangle$ and $\{001\}\langle 100 \rangle$, respectively. In W-5Ta, most grains had normals close to $\mathbf{z} = \langle 011 \rangle$ and $\langle 111 \rangle$, some were close to $\langle 001 \rangle$.

⁵ To produce Fig.1, the formation of visible defects was tracked within a single field-of-view (~ 845 nm by ~563 nm). The issue of loop losses to the surface was circumvented by

Table 2 gives a summary of the defect yield (number of visible loops per ion) and cascade efficiency (fraction of vacancies produced in the collapsed cascades which end up in visible loops) as a function of temperature. Data from previous experiments reported in [8, 13] are included as well as data from repeated runs in the current study. With increasing T_{irr} , the defect yield decreased strongly (from 9.6% to $\leq 0.2\%$), especially above Stage II. Meanwhile, the efficiency of cascade collapse increased (from 9.2% \rightarrow 79%), i.e. more vacancies were retained in the form of loops when cascades collapse.

Fig. 3 shows the frequency of occurrence f per incident ion for loops of size $N(d)$ (the number of point defects in a defect cluster of diameter d). Following the treatments detailed in [8, 49], the conversion from defect diameter d (nm) to cluster size $N(d)$ assumes that all visible defects are circular dislocation loops with $\mathbf{b} = \frac{1}{2} \langle 111 \rangle$ [27]. Hence, $N(d) = \sqrt{3}\pi (d/(2a_0))^2$, where the lattice parameter $a_0 = 0.3165$ nm [50]. Bins in the plot were defined as $[N_i(d - 0.5), N_i(d + 0.5)]$, $i = 1, 2, 3, \dots, 30$, $d = i$ nm, and frequencies f are normalized against the bin width and the total number of W^+ impacts within the regions of interest, to ensure that the areas under the curves in Fig. 3 are equivalent to the total number of point defects counted. Fig. 3 indicates some important points:

(1) In Stage I ($T = 30$ K), the frequency of occurrence f of defect clusters in the range $50 \leq N(d) \leq 500$ obeys a power-law type relationship, i.e. $f \sim A/N(d)^S$, where $A = 2.7 \pm 1.4$, $S = 1.8 \pm 0.1$. When $N(d) > 700$, a pronounced deviation from this relationship is found: f is lower and independent of $N(d)$ to an upper size bound at ~ 1300 [27].

(2) In Stage II ($T = 300$ K), the frequencies of occurrence of small clusters $N(d) < 300$ is lower by a factor of ~ 4 than in Stage I while those of the larger clusters seem unaffected.

(3) A distinct transition takes place in Stage III ($T = 773$ K), where the frequencies of small clusters $N(d) < 300$ are lower than that of Stage II by up to a factor of 100. In addition, the upper size bound shifts to ~ 2000 .

(4) In Stage IV ($T = 1073$ K), a sharp drop in frequency is found for clusters with $200 \leq N(d) \leq 400$, in comparison with Stages I-III. Furthermore, large clusters with $N(d) > 1000$ are more frequently observed and the upper size bound shifts further towards ~ 2300 .

(5) The total number of point defects retained in visible loops (the area under each curve) decreases from 30 K to 1073 K by a factor of around 17. This decrease is most noticeable in the defect size range of $N(d) < 500$.

B-W contrast experiments and image simulations using the TEMACI code [15, 51] enable the identification of defect geometry and nature [13]. Analyses were performed on pure W irradiated at 300 K and 1073 K, on foils with the irradiated surfaces oriented downwards relative to the electron beam, to obtain stronger B-W contrast intensities [10]. Foils were tilted to $\mathbf{z} = [011]$ and dark-field micrographs recorded with $\mathbf{g} = 200$, $\pm (2\bar{1}1)$ and $\pm (21\bar{1})$ strongly excited, as shown in Fig. 4. The contrast of all loops follows $\mathbf{g} \cdot \mathbf{l} > 0$, where \mathbf{l} is the B-W contrast vector, running from the black lobe to that of the white. This is consistent with vacancy loops within 6 nm of the ion entry surface⁶ (see Fig. 3.2 in [51]). At least three variants of $\frac{1}{2} \langle 111 \rangle$ loops are present, as labelled by white markers: circles ($\pm \frac{1}{2} [11\bar{1}]$), parallelograms ($\pm \frac{1}{2} [\bar{1}11]$) and squares ($\pm \frac{1}{2} [\bar{1}11]$ or $\pm \frac{1}{2} [111]$). These identifications can be

counting the total accumulation of freshly formed defects. This procedure was repeated five times and the standard deviation of the mean of these counts is shown as the error bar.

⁶ The same contrast could in principle arise from interstitial loops in the second layer, ≥ 6 nm from the ion-entry surface, where the sign of $\mathbf{g} \cdot \mathbf{l}$ reverses; however, for the irradiation conditions used, corresponding MD simulations [20] predict that most visible loops retained in the foil are within 5-6 nm of the exposed surface.

made with high confidence, according to the $\mathbf{g} \cdot \mathbf{b} = 0$ invisibility criterion and the simple B-W lobe with no interface structure seen when $0 < |\mathbf{g} \cdot \mathbf{b}| \leq 1$ [51].

The loops marked in black were less straightforward to identify. These were visible in all diffraction conditions, and the B-W contrast varied from simple B-W lobes to B-W lobes with interface structure (implying $|\mathbf{g} \cdot \mathbf{b}| > 1$). In Fig. 4 a) where $\mathbf{g} = \bar{2}1\bar{1}$, the loops marked in black show strong B-W lobes with well-defined interface structure, consistent either with $\mathbf{b} = \pm\frac{1}{2}[1\bar{1}1]$ or with $\mathbf{b} = \pm[100]$. The results of image simulations for 1 nm vacancy loops located at depths 2-14 nm beneath the irradiated surface are shown in the supplementary figure, which replicates the imaging condition of Fig. 4 a). Shallower depths were not considered as loops would not remain stable in the foil due to strong surface traction [52]. The foil thickness was measured as ~ 66 nm using EELS. Comparison between simulations and experiment suggest the following matches for these loops: pentagon ($\mathbf{b} = \pm[100]$, $\mathbf{n} = \pm[100]$), triangle ($\mathbf{b} = \pm\frac{1}{2}[1\bar{1}1]$, $\mathbf{n} = \pm[1\bar{1}0]$ or $\pm[101]$) and circle ($\mathbf{b} = \pm\frac{1}{2}[1\bar{1}1]$, $\mathbf{n} = \pm[1\bar{1}1]$), with a best match for a depth position of 2 nm. A similar B-W contrast analysis was carried out for pure W at 1073 K (Fig. 4 f-g). In that case no evidence for $\langle 100 \rangle$ loops was found and nearly all $\frac{1}{2} \langle 111 \rangle$ loops were of pure-edge configuration and were again probably of vacancy nature.

3.2. Microstructural evolution in W and W- 5wt% (Re; Ta; V) alloys at doses 0.1 - 1.0 dpa

In this section, we focus on the evolution of radiation damage in W beyond the cascade overlap dose and how dose, temperature, alloying elements and grain orientation influence damage development.

Damage evolution was monitored constantly during irradiation in all materials to a highest dose of 1.0 dpa. Micrographs were recorded at successively increasing ion doses under WBDF conditions ($\mathbf{g} = 200$, 3-4 \mathbf{g}) in the same area of each specimen (which therefore was illuminated with the electron beam throughout). Detailed post-irradiation characterization to determine defect morphologies and nature, and for quantitative measurements, was then carried out on $\langle 100 \rangle$ oriented specimens of pure W and W- 5wt.% (Re; Ta) irradiated to 1.0 dpa. For the post-irradiation experiments, areas outside the electron beam were chosen, in order to identify any effect of simultaneous electron irradiation on damage development⁷. Dynamical observations during and after irradiation are described in section 3.3.

3.2.1. General evolution of damage microstructures

The top four panels of Fig. 5 illustrate the evolution of damage microstructures in pure W as a function of dose and irradiation temperature. At constant T_{irr} , loop populations always increased with dose. At 300 K, the spatial distribution of loops was random and the average loop size increased somewhat with dose. At $T_{\text{irr}} \geq 773$ K, there was a tendency at doses > 0.4 dpa for loops to order into strings, consisting of several loops arranged linearly, but no networks formed. Some loops within strings were finger-shaped, suggesting that coalescence reactions had taken place. For a given dose, loop number densities decreased strongly with increasing irradiation temperature whilst average loop sizes increased, especially above 773 K, and their spatial inhomogeneity became more marked.

⁷ Areas outside the electron beam were examined only at the end of irradiation (i.e. 1.0 dpa). Imaging lasted 2-3 minutes before the stage was cooled down to room temperature for further detailed characterization. Our earlier work on the in-situ annealing studies of self-ion damaged tungsten [44, 45], indicates that the effects of heating at this temperature on the recovery of visible damage would be negligible during this interval.

The bottom two panels of Fig. 5 show the damage microstructures at 1.0 dpa in W-5 wt.% (Re; Ta). With an increase in irradiation temperature, loop number densities dropped in both alloys and the absolute values became increasingly close to those in pure W for the same irradiation conditions. Average loop sizes were higher in the alloys and were less dependent on temperature. The characteristic strings of loops seen at $T \geq 773$ K in pure W were absent in $\langle 001 \rangle$ grains of alloys, which showed no tendency towards ordering at these irradiation conditions.

In non- $\langle 001 \rangle$ grains, ordering was observed in both pure W and alloys, but the temperature and dose thresholds for this were generally lower than in $\langle 001 \rangle$ grains. This is illustrated for W-5Ta in Fig. 6 a) where damage microstructures in specimens of different grain orientations irradiated at 773 K to 1.0 dpa are presented. The spatial distribution of radiation-induced defects changed from random in the $[001]$ grain towards ordered structures of loop strings and networks in the other orientations. Many small loops were embedded within the networks. In Fig. 6 b), the evolution of such a highly ordered damage microstructure is demonstrated in W-5V irradiated at 1073 K at $z = [011]$. Micrographs were recorded at various stages of the irradiation. At doses ≤ 0.1 dpa, small loops of the same Burgers vector and nature formed, then joined into short strings, and eventually coalesced. At a dose as low as 0.2 dpa, a directionality of loop strings began to emerge: the projected direction of some strings lay close to the $[100]$ direction, whereas others lay within $\pm 30^\circ$ of this direction. Later, we show that loop segments/strings probably contain shear components (see section 3.3.2 and Fig. 11). Network formation occurred at doses ≥ 0.4 dpa, when the loop strings, often now of curly shape, reached moderate length (tens of nm) and density ($\sim 10^{15} \text{ m}^{-2}$).

3.2.2. Evolution of defect populations

Fig. 7 a-c) show areal number densities⁸ averaged over several images in the various materials as a function of irradiation dose and temperature, plotted on a log-log scale. Each set of data has been fitted with one, or in some cases two, straight lines of slope k . In Fig. 7 d), loop number densities at the end of irradiation are compared for different materials, temperatures and for regions under as well outside the electron beam. The following general trends were found:

- 1) with increasing irradiation temperature, the defect population decreased in all materials;
- 2) at all temperatures where the alloying effect was studied, the defect population was highest in W-5Ta, followed by W-5Re and then pure W;
- 3) at 1073 K, the differences in defect population between the alloys were substantially smaller than at 773 K;
- 4) in the presence of an electron beam, the defect population was slightly lower.

In pure W, loop numbers at a dose of 0.1 dpa were lower by around a factor of 27 at 1073 K than at 300 K, and at 1.0 dpa were lower by a factor of 5. At doses ≤ 0.4 dpa, the slope k increased with irradiation temperature. At 300 K and 573 K, k remained constant with values 0.23 and 0.40 respectively throughout the course of irradiation. At $T > 573$ K, the initial rate of damage accumulation at doses ≤ 0.4 dpa was rapid ($k > 1$) and then tended to saturate beyond this dose ($0.2 < k < 0.4$).

⁸ Note that the damage produced by 150 keV W^+ irradiations lies within 40-50 nm of the ion-entry surface according to SRIM, whereas the thicknesses of all the analysed areas of interest were no smaller than this value. This implies that the ‘areal’ number densities of loops would not change with the foil thickness.

In W-5Re, a narrower range of temperature, 773 - 1073 K, was investigated. Absolute defect populations were somewhat higher than in pure W at all doses, and exhibited a weaker but similar temperature dependence. The rates of defect accumulation were similar and low, with $k \sim 0.2$, except initially at 773 K.

In W-5Ta, analyses were also carried out in the range 773 - 1073 K. Absolute defect populations were considerably higher than in pure W and higher than in W-5Re at all doses and around a factor of 2 higher at 773 K than at the higher temperatures. The rates of defect accumulation were both temperature and dose dependent. At doses ≤ 0.4 dpa, the rate of defect accumulation varied within a range $0.2 < k < 0.5$. At higher doses, k decreased to < 0.2 as the damage tended to saturate.

3.2.3. Defect size distributions

Defect size distributions at 1.0 dpa were derived from post-irradiation experiments, and are shown in Fig. 8. In pure W, loops increased in size with increasing irradiation temperature. At $T_{irr} \leq 773$ K, small ≤ 4 nm loops dominated, whereas at 873 K the largest size category was 4-5 nm and at 1073 K it was 5-6 nm. The number of loops in the smallest size category (1-2 nm) decreased sharply from $\sim 27.5\%$ at 573 K to only $\sim 1.5\%$ at 1073 K.

In W-5Re, the size distributions of loops appeared similar at 773 K and 873 K. The largest loop size category in both cases was 1-2 nm, consisting of $\sim 35\%$ of the total loop population. However, at 1073 K the fraction of 1-2 nm loops dropped to $\sim 20\%$ and the largest loop size category was 4-5 nm, making up $\sim 24\%$ of the loop population. At 1073 K the loop number density was much lower than at 873 K, suggesting that fewer loops nucleate at this temperature but more loop growth occurs.

Changes of size distributions in W-5Ta as a function of temperature were minor. The dominant loop size category remained at 1-2 nm, although the fraction of the total loops in this category gradually fell from $\sim 42\%$ to $\sim 30\%$ with increasing T_{irr} . There was some indication that at temperatures above 873 K a decrease in loop number density (see Fig. 5 and Fig. 7 d) was accompanied by an upward shift in loop sizes (Fig. 8). The fraction of 4-5 nm loops increased from $\sim 6\%$ to $\sim 11\%$ between 873 K and 1073 K. Loops ≥ 8 nm were only seen at 1073 K. Ta therefore seems to have a larger effect than Re on restricting loop growth under irradiation.

3.2.4. Defect morphologies

Fig. 9 a) shows the effects of alloying element and irradiation temperature on the fractions of $\frac{1}{2} \langle 111 \rangle$ and $\langle 100 \rangle$ loops at 1.0 dpa. These values were obtained by a statistical approach as described in [27] and references [69,70] therein. In pure W, the fraction of $\frac{1}{2} \langle 111 \rangle$ loops gradually increased with increasing T_{irr} . At 1073 K, almost all loops had $\frac{1}{2} \langle 111 \rangle$ Burgers vectors suggesting that $\langle 100 \rangle$ loops are not thermally stable at high temperatures. In W-5Re the rate of increase in the fraction of $\frac{1}{2} \langle 111 \rangle$ loops with temperature was considerably smaller than in pure W. The fraction of $\frac{1}{2} \langle 111 \rangle$ loops in W-5Ta did not vary much with temperature. At 1073 K, 35% of loops were of $\langle 100 \rangle$ type. This suggests that Re and (especially) Ta may stabilize $\langle 100 \rangle$ loops at elevated temperatures. This is discussed further in section 4.3.

3.2.5. Defect nature

The determination of the interstitial / vacancy nature of $\mathbf{b} = \frac{1}{2} \langle 111 \rangle$ loops was based on inside-outside contrast analysis [51], for loops of diameter ≥ 4 nm (loops smaller than this

could not be reliably analysed). The sampling body consisted up to 150 loops in each material type and the error bars were calculated as the fraction of loops which fell into the 4-5 nm size category which are at the limit of nature determination by this method. Data are shown in Fig. 9 b). The fraction of $\frac{1}{2} \langle 111 \rangle$ loops which were interstitial in nature: 1) was $\sim 50\%$ at irradiation temperatures between 773 K and 873 K in pure W, but increased to 65% at 1073 K; 2) was slightly higher in the alloys than in pure W between 773 K and 873 K, but higher in pure W at 1073 K; 3) gradually increased in W-5Re and W-5Ta throughout the temperature range; 4) was independent of the alloying element (Re, Ta) at this concentration.

However, loops ≥ 4 nm make up in some cases only a small fraction of the total. It should not be assumed that the loops of size < 4 nm are mostly vacancy in nature (as is the case at very low doses). Indirect evidence indicates that at least some of the small mobile $\frac{1}{2} \langle 111 \rangle$ loops are of interstitial type [13, 36].

3.3. The dynamical behaviour of loops

The key sources for understanding the evolution of damage microstructures in tungsten are observations of the dynamical behaviour of loops. At low doses (< 0.4 dpa), the damage microstructure evolved by the *movements of individual loops*, and *loop - loop interactions with close neighbours*. At intermediate doses (0.4 - 1.0 dpa), some loops gathered to form strings, with examples shown in Fig. 5 and Fig. 6. *Loop - string interactions* then become dominant in controlling the microstructure development.

3.3.1. The movements of individual loops

It is known that for Fe an increase in the flux of the high energy bombarding particles (ions or electrons) or an increase in the specimen temperature facilitates the 1D migration of loops, while increases in alloy concentration, irradiation dose and loop size tend to hinder loop movement [33, 53]. The same trends were found here in W and W-alloys. Individual loops were found to exhibit 1D migration in all materials studied. However, the range of the movement and the frequency of migration were heavily dependent upon the presence or absence of the ion beam, the temperature, the irradiation dose, the material and the loop size. We observed striking differences between loops in pure W and W-alloys when the temperature was held constant but the 150 keV W^+ ion beam was blocked. In pure W, 1D migration of loops occurred regardless of the ion beam, whereas in the W-alloys loops remained stationary if the ion beam was blocked. The movement of loops was inhibited as the dose accumulated.

In the supplementary video 1, the 1D migration of a loop in pure W is shown over a period of ~ 30 s, during W^+ ion irradiation at 1073 K. The foil orientation was close to $z = [001]$ and the projected direction of the loop migration was parallel to $\langle 110 \rangle$, suggesting that the Burgers vector of the loop is $\mathbf{b} = \frac{1}{2} \langle 111 \rangle$ [29, 33].

Fig. 10 a) illustrates the influence of temperature on 1D migration of loops with $\mathbf{b} = \frac{1}{2} \langle 111 \rangle$. Several pure W samples were irradiated with 150 keV W^+ ions at 300 K to 1.0 dpa, and were annealed for ~ 30 min at 573 K, 773 K and 1073 K, respectively. The range and frequency of migration were analyzed for loops of comparable diameter (3 - 4 nm). The range of displacement increased by a factor of over 3 from 0 - 2.5 nm at 573 K to 0 - 8 nm at 773 K and 1073 K. At 773 K especially, displacements were often accomplished in several discrete steps or hops, producing shoulders on the sides of the displacement peaks. This observation suggests that the ambient temperature affects not only the diffusion rate of loops, but also shapes the interacting environment by varying the population of defects which impede loop motion.

The interstitial or vacancy nature of the hopping loops could not be directly determined. According to MD simulations, both interstitial loops and vacancy loops of $\frac{1}{2} \langle 111 \rangle$ type are expected to be mobile from Stage II, envisaged as the collective motion of a bundle of crowdions or ‘voidions’ [54] along the closest packed direction $\langle 111 \rangle$. However the loops which hopped during the experiments are more likely to be interstitial type, since their migration barrier is estimated to be ~ 0.01 eV [55], lower by an order of magnitude than for vacancy loops (0.13 eV [8]).

1D migration of $\langle 100 \rangle$ loops was not observed. These loops tended to act as sessile traps for smaller loops or clusters [13]. An estimate given in [45] showed that it takes ~ 1 hour for a $\langle 100 \rangle$ loop to achieve a displacement of 1 nm at 1473 K through vacancy-mediated climb. At higher temperatures they seem to be thermally unstable (and so were largely absent in Stage IV as suggested in Fig. 9 b).

3.3.2. Loop - loop and loop - string interactions

Loops of the same Burgers vector (of type $\frac{1}{2} \langle 111 \rangle$) and interstitial nature tended to align by mutual elastic interaction [13, 44] (see supplementary video 2). Similar observations have been made in Fe, where sometimes long chains of loops were seen to perform an elaborate dance [34-36]. If sufficiently close, loop coalescence may take place, giving large, often finger-shaped products.

Fig. 10 b) shows a pure W sample, irradiated at 1073 K close to $\mathbf{z} = [001]$. Loop A (\uparrow) with $\mathbf{b} = \pm \frac{1}{2} [\bar{1}\bar{1} \pm 1]$ is seen to glide back and forth on its glide cylinder (projected in the $[\bar{1}\bar{1}0]$ direction) towards a neighbouring group of loops. This 1D motion repeats until eventually the loop joins the string. In Fig. 10 c), in the same specimen, two loops with $\mathbf{b} = \pm \frac{1}{2} [\bar{1}\bar{1} \pm 1]$ coalesce into a larger loop with the same Burgers vector. The entire process was completed within 0.33s.

A more complex example of loop-loop and loop-string interaction, in a W-5V sample irradiated at 1073 K close to $\mathbf{z} = [011]$ is shown in Fig. 11 and supplementary video 3. Three major changes occurred in the frames presented (Fig. 11 a-b):

- 1) 0.00s \sim 0.07s, loop C (\blacktriangleright) rotated $\sim 30^\circ$ to coalesce with loop D (\blacktriangleleft), forming loop A;
- 2) 7.73s \sim 8.00s, loop A and loop E (\uparrow) gradually joined into a single string, A';
- 3) 8.00s \sim 9.00s, loop F (\blacktriangledown) hopped along $[0\bar{1}1]$, and joined string A' to form string B.

All loops involved in this coalescence process (A to F) must be of the same nature, almost certainly interstitial, since the length of the string increased after each step. Based on the $\mathbf{g}\cdot\mathbf{b}$ criterion [56], the $\frac{1}{2} \langle 111 \rangle$ loops visible in $\mathbf{g} = 0\bar{1}1$ are $\mathbf{b} = \pm \frac{1}{2} [\bar{1}\bar{1}1]$ and $\pm \frac{1}{2} [\bar{1}\bar{1}\bar{1}]$. Image simulations using the TEMACI code [15] were performed for loops of these Burgers vectors, with four different habit planes to treat cases of pure-edge loops and loops containing shear components (Fig. 11 c). All loops were assumed to be of diameter 10 nm, located at 15 nm beneath the upper surface in a 100 nm foil. String B is made up of string A' and loop F. String A' fits best with the contrast of $\frac{1}{2} [\bar{1}\bar{1}1]$ loops lying on $(\bar{1}01)$ or $(\bar{1}\bar{1}0)$ while loop F matches well with that of $\frac{1}{2} [\bar{1}\bar{1}\bar{1}]$ loops lying on $(\bar{1}\bar{1}1)$. Consistent with this, the angle between string A' and loop F is close to 35° . Hence, it is probable that the morphology of string B is a result of the coalescence between a pure-edge loop and a string of loops with shear components. It is therefore not necessary for the habit planes of loops to rotate in order for coalescence to proceed. This could account for the geometrical features of dislocation networks seen in W-5Ta and W-5V samples (Fig. 6), where the projected direction of loop strings were often not perpendicular to $\langle 110 \rangle$ directions.

4. Discussion

4.1. Cascade damage production and evolution in tungsten

The lowest-dose (≤ 0.01 dpa) investigations in this study can be categorized as exploring high temperature⁹ “near-surface” cascade effects. Defect clusters formed at individual cascade sites in the form of dislocation loops, most likely of vacancy nature, and of size up to $N \sim 1300$ point defects. Recent studies of Osetsky et al. [57] suggest these clusters could be the consequence of a destructive supersonic shock front interacting with the free surface. The upper bound for defect cluster size is probably associated with the onset of a cascade branching phenomenon; the threshold cascade energy for cascade branching in tungsten is just above 150 keV [18]. Although most loops were of $\frac{1}{2} \langle 111 \rangle$ type, a substantial minority of $\langle 100 \rangle$ loops was also present. This observation is in good agreement with the predictions of the Eyre-Bullough mechanism [16] as well as with MD simulations [18, 58]. MD also predicts the presence of mixed loops (combining $\langle 111 \rangle$ and $\langle 100 \rangle$ components) but none were found in the experiments: this is likely to reflect free-energy driven evolution of the loops between the quench-phase and equivalent MD predictions [18, 58] (~ 10 ps) and the annealing phase and TEM observations (\sim ms) [58, 59].

The most distinct change in behaviour with increasing irradiation temperature from Stage I ($T_{\text{irr}} = 30$ K) [49] to Stage IV ($T_{\text{irr}} = 1073$ K) is a significant fall-off in retained point-defect concentration (by a factor of 17) inferred from the size measurements of visible loops (Figs. 2 and 3). This decrease may be because irradiations at higher temperatures result in slower cooling rates of the cascade core, and hence an extended thermal spike lifetime and increased chances of point defect recombination in this phase [58]; further factors are elastic interactions within individual cascades over the annealing phase and the presence of a strong surface sink in the vicinity of these cascades.

Mason et al. [8] demonstrated the impact of these factors with okMC simulations. The evolution of point-defects and clusters surviving after the collisional phase of 150 keV W^+ cascades was followed to ~ 10 s in a 40 nm foil. Those which were then left were voids or loops deeply trapped by neighbouring clusters. The majority of clusters which nucleated were glissile $\frac{1}{2} \langle 111 \rangle$ loops. The elastic interaction energies U of small loops with neighbouring clusters are small ($U \propto A_1 A_2$, where A_1 and A_2 are loop areas [60]), and may not counter-balance the surface traction, so that many may be lost to the surface. However, larger loops have larger mutual elastic interaction energies (on average > 6 eV for $\bar{N}(d) \sim 800$) and so may be retained in the foil. These considerations may account at least partially for the experimental observations. Also, density functional theory (DFT) calculations have implied that a void (3D) configuration is more stable than a loop (2D) configuration for vacancy clusters in tungsten [61]. Accordingly, they may have undergone configurational transformations towards voids in high temperature irradiations, which can be challenging to resolve reliably by TEM when $N(d) < 260$ [8, 51]¹⁰.

Another effect of irradiation temperature was a shift towards larger loop sizes in cluster size distributions. In Stage I (30 K) and II (300 K) the size distributions were similar for $N(d) > 500$, most likely as a result of weak elastic attraction between clusters in the same cascade, which prohibited size increases through collisions and subsequent coalescence. In Stage III (773 K), the diffusivity of small clusters is higher, favouring both losses to the surface and loop coalescence, leading to fewer but larger loops. In Stage IV (1073K), the size distributions showed a dramatic drop in the number of clusters in the size range $100 \leq N(d) \leq$

⁹ For a comparable low temperature (30K) study, see [49].

¹⁰ Note that the smallest and accurately resolvable size of a void is ~ 2 nm, which is equivalent to ~ 260 vacancies. Voids of image size ~ 1 nm are detectable, but sizing would not be reliable.

500 but little change for $N(d) < 100$. TEM at this stage showed that loops in pure W increased in image contrast brightness and size over a time ~ 0.3 s. These observations are most likely associated with the elastic interaction and coalescence of clusters of intermediate or large size produced in the same cascade, where the mutual elastic attraction is larger than for pairs of clusters where at least one is small. The okMC simulations of Mason et al. showed that growth by the absorption of single vacancies at loop peripheries would be orders of magnitude slower than those observed [8]. This mechanism does result in an increase in cluster size in Stage III, but the magnitude of the predicted size increase is far less than seen experimentally.

Fig. 4 demonstrates that pure-edge $\frac{1}{2} \langle 111 \rangle$ loops are the most stable defect configuration at high temperatures. Once formed on $\{110\}$ planes, $\frac{1}{2} \langle 111 \rangle$ loops with shear components may simply transform into pure-edge configuration through the rotation of their habit planes towards $\{111\}$. However, the elimination path of $\langle 100 \rangle$ loops at high temperatures remains unclear.

4.2. Dynamic behaviour of loops

MD simulations have indicated that small migrating loops in pure tungsten are essentially bundles of $\langle 111 \rangle$ crowdions in 1D collective Brownian motion [55]. Such configurations are very mobile. However the energetic landscape which a migrating loop sees in a real material is different to that simulated by MD, and it varies as a function of time. In a real material a migrating loop would be immersed in a sea of elastically interacting small clusters, impurities and alloying atoms. The observations of motion consisting of a series of infrequent and instantaneous hops separated by finite intervals of time described in section 3.3 are consistent with this “elastic trapping” hypothesis and are crucial for picturing the damage evolution.

The 1D migration of loops may have two consequences. If the glide cylinder intersects with the foil surface, the loop might be lost if it lies insufficiently deep in the foil or is not trapped by neighbouring defects. If the glide cylinder lies parallel to the foil surface, loops may undergo correlated 1D motion due to the interactions between their strain fields, provided the loop separation distance R is comparable with the loop diameter [60]. Real-time Langevin dynamic simulations have shown that this correlated motion most likely involves $\frac{1}{2} \langle 111 \rangle$ loops of the same Burgers vector variant, for which the width and the depth of the interaction potential well is largest [40], giving rise to stable and stationary chains or strings of loops as shown in Figs. 5 and 10 b).

Following the formation of chains of interstitial $\frac{1}{2} \langle 111 \rangle$ loops of collinear geometry, coalescence into large “finger-shaped” loops of the same Burgers vector was sometimes found in $\mathbf{z} = \langle 001 \rangle$ grains of pure W irradiated at $T > 773$ K, and was frequently seen in non $\mathbf{z} = \langle 001 \rangle$ grains of alloyed samples. The direction of loop growth follows that of the climb axis (close to the $[110]$ direction in Fig. 10 c), indicating that a conservative (self) climb process of two reacting loops has most likely taken place [62]. In addition, the resulting finger loops often featured curved (Fig. 10 b) or curly morphologies (Figs. 6 and 11). The presence of curved morphologies indicates that the loop motion may have also involved glide, in order to accommodate stresses induced by the bombarding W^+ ions and electrons, as postulated for similar observations in iron [34, 35]. The curly morphologies originate from the coalescence of collinear loops with different habit planes, as shown by TEMACI simulations in Fig. 11 c), which brings about a so-called “stepped” geometry for the habit planes of product loops [34].

Nanometre-sized loop-loop reactions in self-ion irradiated tungsten can also involve the combination of different variants of $\frac{1}{2} \langle 111 \rangle$ loops, as well as reactions of $\langle 100 \rangle$ loops with $\frac{1}{2} \langle 111 \rangle$ loops. Despite the wide variety of geometric combinations, the product tended always to adopt the Burgers vector of the larger reactant [30]. Similarly, large finger loops

often absorbed nearby non-collinear loops. Such reactions were also responsible for the evolution of most defect clusters located away from the spatially ordered structures of interstitial $\frac{1}{2} \langle 111 \rangle$ loops. It is in such regions that isolated interstitial $\langle 100 \rangle$ loops and most $\frac{1}{2} \langle 111 \rangle$ vacancy loops were identified.

4.3. Factors influencing microstructural evolution

Irradiation parameters and chemical composition play crucial roles in driving microstructural evolution by altering the kinetics and thermodynamics of radiation defects. In this section, we discuss microstructural evolution mechanisms explicitly in $\mathbf{z} = \langle 001 \rangle$ grains from the following aspects: evolution of defect population, defect clustering behaviour and defect morphologies.

Figs. 1 and 7 show loop densities as a function of irradiation dose on log-log scales: the process of loop production may be characterised by the slope k of such graphs. As noted in section 3.1, a value $k=1$ indicates that the loop density is proportional to the irradiation dose and is characteristic of early-stage damage where the visible defects are produced by the collapse of the vacancy-rich cores of individual cascades (Fig.1, ≤ 0.01 dpa). A value $k < 1$ is typical of later stages of damage production, section 3.2.2 and Fig.7, when loop populations increase more slowly with dose and eventually approach saturation, often by means of loop reactions [33, 63]. The regime $k > 1$ corresponds to copious loop production by nucleation of new loops both within cascades, and in inter-cascade regions by point defects and small clusters which have escaped cascades.

The pure W data in Fig. 7 a) shows all three scenarios. In Stage II (300 K, 573 K), $k < 1$. In this stage the loop populations are high compared to Stages III-V (see also Fig. 2) and are close to saturation. Few new loops nucleate, probably because the loop average separations are small and cascade debris created by new bombarding ions is mostly absorbed by existing loops. Loop coalescence reactions, if present at all, remain localized. In Stage III (773 K, 873 K), where $k > 1$ at low doses, the absolute loop populations are about an order of magnitude smaller than in Stage II. Most visible loops are well separated and elastic interactions among them are likely to be negligible. Nucleation of new loops occurs readily, many are retained in the foil, and the loop population increases rapidly. However, at around 0.4 - 0.6 dpa ($4 - 6 \times 10^{17} \text{ W}^+ \text{m}^{-2}$), k drops significantly to ~ 0.27 . This is probably an indication of increased loop reactions corresponding to increasingly correlated 1D motion of $\frac{1}{2} \langle 111 \rangle$ loops and their merging into large finger loops. These large loops absorb a majority of the freshly nucleated loops and impede further loop accumulation. As discussed in section 4.2, such behaviour is expected when the loop density and loop mobility are sufficiently high, which is the case in this temperature/dose regime. Similar interpretations can be applied to Stage IV (1073 K).

The presence of Re and Ta in tungsten resulted in consistently higher loop densities but smaller mean loop sizes, and a rapid saturation of loop densities with dose. More pronounced effects were found in W-Ta than in W-Re. Consistent with this, nano-indentation studies on the same irradiated materials have shown that the more defective irradiated W-5Ta demonstrates greater hardening than W-5Re [27, 46, 64]. These effects may be due to several related mechanisms:

- (1) Solute atoms such as Re and Ta might interact with radiation-induced point defects. DFT calculations predict attractive interactions for Re-vacancy (~ 0.3 eV), Re-crowdion (0.82 eV, // $\langle 111 \rangle$ direction; ~ 0.5 eV, \perp $\langle 111 \rangle$ direction) and Ta-crowdion (~ 0.2 eV, \perp $\langle 111 \rangle$ direction), a repulsive interaction for Ta-crowdion (~ 0.6 eV, // $\langle 111 \rangle$ direction) and negligible interaction for Ta-vacancy [65, 66]. Overall during the cascade cooling phase, the formation of mixed point defect-solute atom configurations would likely be favoured

over SIAs and vacancies. The thermal stability of these mixed configurations may reduce the recombination rate and increase cluster nucleation.

- (2) The presence of impurities might affect the probability that defect clusters of both interstitial and vacancy nature transform to planar loops. According to the Eyre-Bullough mechanism, the initial configuration of loops in b.c.c. metals is faulted [16], in which case their nucleation probability would be determined by the stacking fault energy (SFE). Substitutional elements like Re and Ta may segregate to faults and reduce the SFE, so boosting the probability of loop formation [67].
- (3) Long-range diffusion of clusters might be impeded by solute atoms. Experimental evidence for this was found in this work: small loops in pure W were very mobile, but 1D migration of small loops was strongly inhibited in alloys (see section 3.4.1). Consequently, damage development would be less determined by loop interactions and reactions in the alloys than in pure W, and the microstructure thus rapidly saturates with newly-formed loops.

The above mechanisms would all lead to a higher number of smaller defect clusters in W-alloys than in pure W. These mechanisms have not yet been investigated theoretically in W-based alloys; however analogous mechanisms have been reported by Malerba et al in cascade simulations of pure Fe and Fe-10Cr [68] for PKA energies up to 15 keV (below the threshold for subcascade formation [57]). In that work, higher numbers of Frenkel pairs survived in cascades in Fe-10Cr than in pure Fe due to the production of stable mixed dumbbells. The fraction of defects in clusters was found to be similar in the alloy but cluster mobilities were found to be substantially lower.

At this time the reasons why Ta has a larger effect than Re on damage development is not understood. DFT studies of binding energies referenced above suggest that Re interacts with point defects more than Ta, in apparent contradiction with the experimental observations. The discrepancy here originates from the significant difference in time- and length-scales. MD simulations of collision cascades in W-5Re and W-5Ta, coupled with a coarse-grain simulation methodology like oKMC or Langevin dynamics are needed, in order to account for the interactions of loop-solutes, loop-loops, solute-solutes and point defect - solutes over experiment-relevant time-scales.

Defect morphologies are strongly dependent on the irradiation temperature, as demonstrated in Fig. 9 a). The fraction of $\frac{1}{2} \langle 111 \rangle$ loops in pure W increased with increasing irradiation temperature and at 1073 K, nearly all loops were found to be $\frac{1}{2} \langle 111 \rangle$ type. Gilbert [69] interpreted this trend in terms of free energy, which increases with temperature for both $\frac{1}{2} \langle 111 \rangle$ and $\langle 100 \rangle$ loops in pure W, but at a much slower rate for $\frac{1}{2} \langle 111 \rangle$ loops. The presence of solute atoms also affected the loop morphologies: Re and especially Ta appeared to undermine this thermodynamic preference for $\frac{1}{2} \langle 111 \rangle$ loops. Taking solute-solute and solute-loop interactions into account [65, 66], it would be expected that Re atoms would prefer to bind strongly to loop peripheries (direction parallel with the loop plane normal) [70], while Ta atoms would tend not to segregate, but would be weakly bound to the loop peripheries (direction parallel with the loop plane). In either case it is likely that the overall free energy of the loop-solute configuration may have altered, possibly more significantly in loops decorated with individual solute atoms.

The effects of grain orientations and the presence or absence of the electron beam during irradiation on microstructural evolution are likely to be due to interactions between radiation defects and the specimen surface. In non $z = \langle 001 \rangle$ grains, loops with different Burgers vector variants are lost to the surface with different probabilities. If the loop glide cylinder does not intersect the surface, loops of that variant will be retained. This leads to biased loop geometries as detailed in [27]. The spatial ordering of collinear $\frac{1}{2} \langle 111 \rangle$ loops can likewise be facilitated, due to the removal of traps along their in-plane glide cylinders. Consequently,

the threshold dose and temperature for loop strings to be observed can be significantly lower in non $\mathbf{z} = \langle 001 \rangle$ (doses ≤ 0.1 dpa; $T \leq 773$ K; estimates based on Fig. 6 a-b). A sub-threshold electron beam (< 500 keV [71]) may de-trap loops weakly bound to impurities and possibly even small point defect clusters, favouring their loss to the surface by glide. This probably accounts for the 10-20% difference in loop number densities shown in Fig. 7 d) between regions under and outside the electron beam.

4.4. Thin-foil versus near-bulk irradiations

Thin-foil and near-bulk irradiations differ in various aspects: the vicinity of the free surface; the PKA energies, and hence the concentration and spatial distribution of the damage; and different production rates of radiation defects. We may compare the thin-foil experiments using 150 keV W^+ irradiations of this work with 2 MeV W^+ irradiations of the same materials at the same irradiation temperatures, doses and grain orientations [27]. Despite the differences listed above, the general trends with irradiation temperature and alloying composition in loop densities, overall size distributions, relative fractions of $\frac{1}{2} \langle 111 \rangle$ loops over $\langle 100 \rangle$ loops and of interstitial loops over vacancy loops were qualitatively remarkably similar. Similar complex features such as loop strings, rafts and networks were found in both cases, and the threshold condition for these to appear were comparable, e.g. doses $> (0.4 \sim 1.0) \times 10^{18} \text{ W}^+ \text{m}^{-2}$, $T \geq 773$ K for $\mathbf{z} = \langle 001 \rangle$ grains of pure W. Quantitatively, the fractions of $\frac{1}{2} \langle 111 \rangle$ loops and the fractions of these $\frac{1}{2} \langle 111 \rangle$ loops which were interstitial were within a factor of two, as demonstrated in Fig. 12. The fact that a higher proportion of $\frac{1}{2} \langle 111 \rangle$ interstitial loops was found in the near-bulk samples suggests less loss of such loops to the free surface, and so would be more representative of bulk behaviour. However we may have some confidence that the trends seen in thin foil in-situ experiments are relevant to the bulk behaviour under ion irradiation.

5. Conclusions

A comprehensive study has been carried out of radiation damage production and microstructural evolution in pure W and W-5wt.% (Re, Ta) alloys resulting from in-situ 150 keV W^+ ion irradiations; qualitative damage evolution was also studied in a W-5wt.%V alloy. Detailed defect characterization demonstrated the roles of irradiation temperature, dose, alloying and grain orientations. We have found that:

1. Both $\frac{1}{2} \langle 111 \rangle$ and $\langle 100 \rangle$ loops were present within individual cascades in pure W (≤ 0.01 dpa, 30 - 1073 K), and they were most likely of vacancy nature.
2. The irradiation temperature had a pronounced impact on damage development within individual cascades in W. From 30 K to 1073 K, the concentration of point defects retained in loops decreased by a factor of 17. Loop sizes increased markedly from Stage III as a result of elastic interaction and coalescence reactions. Pure-edge $\frac{1}{2} \langle 111 \rangle$ configurations were found the most thermally favoured loop geometry. At 1073 K, nearly all loops were of this type.
3. At higher doses, the dynamic behaviour of defects profoundly influenced microstructural development. Notably, loop strings and networks formed from the correlated 1D migration of $\frac{1}{2} \langle 111 \rangle$ interstitial loops with collinear geometry, and their subsequent coalescence. Loop-loop reactions between non-collinear Burgers vector combinations also occurred, and were responsible for the formation of isolated $\langle 100 \rangle$ interstitial loops and nearly all vacancy loops embedded in regions between the spatially ordered structures.

4. Alloying elements (Re, Ta) increased loop densities, which tended to saturate early in the irradiation, and restricted loop growth. Alloying also affected the relative thermal stability of $\frac{1}{2}$ $\langle 111 \rangle$ and $\langle 100 \rangle$ loops. A higher fraction of $\langle 100 \rangle$ loops was present in W-5Ta and W-5Re than in pure W. Non $\mathbf{z} = \langle 001 \rangle$ grain orientations favoured the spatial ordering of loops, probably as a result of a changed bias on the geometries of loops retained in the foil.
5. In-situ experiments showed consistent trends in damage production and microstructural evolution with 2 MeV W^+ near-bulk irradiations of the same materials.

Acknowledgements

The electron microscopy with in-situ ion irradiation was carried out at Argonne National Laboratory at the IVEM-Tandem Facility, a U.S. Department of Energy Facility funded by the DOE Office of Nuclear Energy, operated under Contract No. DE-AC02-06CH11357 by UChicago Argonne, LLC. We thank Pete Baldo and Edward Ryan for their help with the irradiations. XY thanks Prof. Sergei Dudarev, Dr. Daniel Mason, Dr. Duc Nguyen-Manh and Dr. Mark Gilbert for fruitful discussions, and the Culham Centre for Fusion Energy for funding via a Junior Research Fellowship at St Edmund Hall, University of Oxford. XY, MLJ and SGR acknowledge support from the EPSRC via the programme grant “Materials for Fusion and Fission Power”, EP/H018921/1.

Supplementary materials

Video 1: 1D migration of a $\frac{1}{2}$ $\langle 111 \rangle$ loop in pure W (as labelled) during irradiation with 150 keV W^+ ions at 1073 K, close to $\mathbf{z} = [001]$ orientation.

Video 2: Correlated motion of two $\frac{1}{2}$ $\langle 111 \rangle$ loops (as labelled) in pure W, both during (first 17s) and after (17s - the end) 150 keV W^+ ion bombardment at 1073 K.

Video 3: Loop string formation in W-5V as a result of the 1D migration of $\frac{1}{2}$ $\langle 111 \rangle$ loops with different habit planes. Irradiation condition: 150 keV W^+ ions, $\mathbf{z} = [011]$, 1073 K.

Supplementary figure: Image simulations (TEMACI code) were performed on the black-white contrasts of vacancy loops in tungsten, in order for comparison with the experimental data shown in Fig. 4. The simulations were for a $\mathbf{b} = [100]$ loop and four variants of $\mathbf{b} = \frac{1}{2}\langle 111 \rangle$ loops in a foil of 66 nm with $\mathbf{z} = [011]$. Loop depth 52 - 64 nm; loop diameter 1 nm; loop normal \mathbf{n} ; diffraction condition $\mathbf{g} = \bar{2}1\bar{1}$.

References

- [1] M.R. Gilbert, S.L. Dudarev, S. Zheng, L.W. Packer, J.-C. Sublet, An integrated model for materials in a fusion power plant: transmutation, gas production, and helium embrittlement under neutron irradiation, *Nucl. Fusion*. 52 (2012) 083019.
- [2] M.R. Gilbert, J.-C. Sublet, Neutron-induced transmutation effects in W and W-alloys in a fusion environment, *Nucl. Fusion* 51 (2011) 043005.
- [3] S.J. Zinkle, G.S. Was, Materials challenges in nuclear energy, *Acta Mater.* 61 (2013) 735-758.
- [4] C.-Y. Wei, D.N. Seidman, The spatial distribution of self-interstitial atoms around depleted zones in tungsten ion-irradiated at 10 K, *Philos. Mag. A*. 43 (1981) 1419-1439.
- [5] C.-Y. Wei, M.I. Current, D.N. Seidman, Direct observation of the primary state of damage of ion-irradiated tungsten I. Three-dimensional spatial distribution of vacancies, *Philos. Mag. A*. 44 (1981) 459-491.

- [6] M.I. Current, C.-Y. Wei, D.N. Seidman, Direct observation of the primary state of damage of ion-irradiated tungsten. II. Definitions, analyses and results, *Philos. Mag. A.* 47 (1983) 407-433.
- [7] R.M. Scanlan, D.L. Styris, D.N. Seidman, An in situ field ion microscope study of irradiated tungsten, *Philos. Mag.* 23 (1971) 1439-1457.
- [8] D.R. Mason, X. Yi, M.A. Kirk, S.L. Dudarev, Elastic trapping of dislocation loops in cascades in ion-irradiated tungsten foils, *J. Phys: Condens. Matter.* 26 (2014) 375701.
- [9] F. Häussermann, M. Rühle, M. Wilkens, Black-white contrast figures from small dislocation loops II. Application of the first order solution to small loops in ion-irradiated tungsten foils, *Phys. Stat. Sol. (b)* 50 (1972) 445-457.
- [10] F. Häussermann, Analysis of dislocation loops in tungsten produced by 60keV ion irradiation, *Philos. Mag.* 25 (1972) 561-581.
- [11] F. Häussermann, A study of the radiation damage produced by energetic gold ions in molybdenum and tungsten, *Philos. Mag.* 25 (1972) 583-598.
- [12] W. Jäger, M. Wilkens, Formation of vacancy-type dislocation loops in tungsten bombarded by 60 keV Au ions, *Phys. Stat. Sol. (a)* 32 (1975) 89-100.
- [13] X. Yi, M.L. Jenkins, M. Briceno, S.G. Roberts, Z. Zhou, M.A. Kirk, In situ study of self-ion irradiation damage in W and W-5Re at 500 °C, *Philos. Mag.* 93 (2012) 1715-1738.
- [14] TEMACI: A computer program for TEM amplitude contrast imaging., Oxford, 2005. <http://www.materials.ox.ac.uk/research/publications/temaci.html>.
- [15] Z. Zhou, M.L. Jenkins, S.L. Dudarev, A.P. Sutton, M.A. Kirk, Simulations of weak-beam diffraction contrast images of dislocation loops by the many-beam Howie–Basinski equations, *Philos. Mag.* 86 (2006) 4851-4881.
- [16] B.L. Eyre, R. Bullough, On the formation of interstitial loops in b.c.c. metals, *Philos. Mag.* 12 (1965) 31-39.
- [17] Y. Zhong, K. Nordlund, M. Ghaly, R.S. Averback, Defect production in tungsten: A comparison between field-ion microscopy and molecular-dynamics simulations, *Phys. Rev. B.* 58 (1998) 2361-2364.
- [18] A.E. Sand, S.L. Dudarev, K. Nordlund, High-energy collision cascades in tungsten: Dislocation loops structure and clustering scaling laws, *EPL* 103 (2013) 46003.
- [19] O.V. Ogorodnikova, V. Gann, Simulation of neutron-induced damage in tungsten by irradiation with energetic self-ions, *J. Nucl. Mater.* 460 (2015) 60-71.
- [20] A.E. Sand, K. Nordlund, S.L. Dudarev, Radiation damage production in massive cascades initiated by fusion neutrons in tungsten, *J. Nucl. Mater.* 455 (2014) 207-211.
- [21] K.M. Bowkett, B. Ralph, The Annealing of Radiation Damage in Tungsten Investigated by Field-Ion Microscopy, *Proc. R. Soc. A* 312 (1969) 51-63.
- [22] L.K. Keys, J. Moteff, Neutron irradiation and defect recovery of tungsten, *J. Nucl. Mater.* 34 (1970) 260-280.
- [23] A. Hasegawa, M. Fukuda, T. Tanno, S. Nogami, Neutron Irradiation Behavior of Tungsten, *Mater. Trans.* 54 (2013) 466-471.
- [24] A. Hasegawa, M. Fukuda, S. Nogami, K. Yabuuchi, Neutron irradiation effects on tungsten materials, *Fus. Eng. Des.* 89 (2014) 1568-1572.
- [25] T. Tanno, A. Hasegawa, J.-C. He, M. Fujiwara, S. Nogami, Effects of transmutation elements on neutron irradiation hardening of tungsten, *Mater. Trans.* 48 (2007) 2399-2402.
- [26] Ł. Ciupiński, O.V. Ogorodnikova, T. Płociński, M. Andrzejczuk, M. Rasiński, M. Mayer, K.J. Kurzydłowski, TEM observations of radiation damage in tungsten irradiated by 20 MeV W ions, *Nucl. Instrum. Methods Phys. Res. B.* 317, Part A (2013) 159-164.
- [27] X. Yi, M.L. Jenkins, K. Hattar, P.D. Edmondson, S.G. Roberts, Characterisation of radiation damage in W and W-based alloys from 2 MeV self-ion near-bulk implantations, *Acta Mater.* 92 (2015) 163-177.

- [28] R.E. Smallman, *Modern Physical Metallurgy* (Butterworths Monographs in Metals), 4th ed., Butterworth-Heinemann, London, 1985.
- [29] K.Arakawa, K.Ono, M.Isshiki, K.Mimura, M.Uchikoshi, H.Mori, Observation of the One-Dimensional Diffusion of Nanometer-Sized Dislocation Loops, *Science* 318 (2007) 956-959.
- [30] K. Arakawa, T. Amino, H. Mori, Direct observation of the coalescence process between nanoscale dislocation loops with different Burgers vectors, *Acta Mater.* 59 (2011) 141-145.
- [31] K. Arakawa, M. Hatanaka, E. Kuramoto, K. Ono, H. Mori, Changes in the Burgers Vector of Perfect Dislocation Loops without Contact with the External Dislocations, *Phys. Rev. Lett.* 96 (2006) 125506.
- [32] K. Arakawa, H. Mori, Energetics of formation process of a prismatic dislocation loop via the collision between two $1/2$ loops in α -iron, *J. Phys.: Conf. Ser.* 165 (2009) 012005.
- [33] Z. Yao, M. Hernández-Mayoral, M.L. Jenkins, M.A. Kirk, Heavy-ion irradiations of Fe and Fe–Cr model alloys Part 1: Damage evolution in thin-foils at lower doses, *Philos. Mag.* 88 (2008) 2851-2880.
- [34] M. Hernández-Mayoral, Z. Yao, M.L. Jenkins, M.A. Kirk, Heavy-ion irradiations of Fe and Fe–Cr model alloys Part 2: Damage evolution in thin-foils at higher doses, *Philos. Mag.* 88 (2008) 2881-2897.
- [35] M.L. Jenkins, Z. Yao, M. Hernández-Mayoral, M.A. Kirk, Dynamic observations of heavy-ion damage in Fe and Fe–Cr alloys, *J. Nucl. Mater.* 389 (2009) 197-202.
- [36] Z. Yao, M.L. Jenkins, M. Hernández-Mayoral, M.A. Kirk, The temperature dependence of heavy-ion damage in iron: A microstructural transition at elevated temperatures, *Philos. Mag.* 90 (2010) 4623-4634.
- [37] M. Li, M.A. Kirk, P.M. Baldo, D. Xu, B.D. Wirth, Study of defect evolution by TEM with in situ ion irradiation and coordinated modeling, *Philos. Mag.* 92 (2012) 2048-2078.
- [38] M.R. Gilbert, Z. Yao, M.A. Kirk, M.L. Jenkins, S.L. Dudarev, Vacancy defects in Fe: Comparison between simulation and experiment, *J. Nucl. Mater.* 386-388 (2009) 36-40.
- [39] D. Xu, B.D. Wirth, M. Li, M.A. Kirk, Combining in situ transmission electron microscopy irradiation experiments with cluster dynamics modeling to study nanoscale defect agglomeration in structural metals, *Acta Mater.* 60 (2012) 4286-4302.
- [40] S.L. Dudarev, K. Arakawa, X. Yi, Z. Yao, M.L. Jenkins, M.R. Gilbert, P.M. Derlet, Spatial ordering of nano-dislocation loops in ion-irradiated materials, *J. Nucl. Mater.* 455 (2014) 16-20.
- [41] S.L. Dudarev, M.R. Gilbert, K. Arakawa, H. Mori, Z. Yao, M.L. Jenkins, P.M. Derlet, Langevin model for real-time Brownian dynamics of interacting nanodefects in irradiated metals, *Phys. Rev. B.* 81 (2010) 224107.
- [42] M.R. Gilbert, J. Marian, J.-C. Sublet, Energy spectra of primary knock-on atoms under neutron irradiation, *arXiv:1506.08554 [cond-mat.mtrl-sci]* (2015)
- [43] Tungsten powder purity, Plansee Gruppe, Austria, 2014.
<http://www.plansee.com/en/Materials-Tungsten-403.htm#Wolframrhenium>.
- [44] X. Yi, M.L. Jenkins, M.A. Kirk, S.G. Roberts, In-situ annealing of self-ion irradiation damage in tungsten, *MRS Symp. Proc.* 1712 (2014) DOI: 10.1557/opl.2014.1732.
- [45] F. Ferroni, X. Yi, K. Arakawa, S.P. Fitzgerald, P.D. Edmondson, S.G. Roberts, High temperature annealing of ion irradiated tungsten, *Acta. Mater.* 90 (2015) 380-393.
- [46] D.E.J. Armstrong, X. Yi, E.A. Marquis, S.G. Roberts, Hardening of self ion implanted tungsten and tungsten 5-wt% rhenium, *J. Nucl. Mater.* 432 (2013) 428-436.
- [47] J. Reiser, M. Rieth, B. Dafferner, A. Hoffmann, X. Yi, D.E.J. Armstrong, Tungsten foil laminate for structural divertor applications – Analyses and characterisation of tungsten foil, *J. Nucl. Mater.* 424 (2012) 197-203.

- [48] N.M. Ghoniem, Atomic processes during damage production and defect retention, *J. Nucl. Mater.* 258-263, Part 1 (1998) 113-123.
- [49] X. Yi, A.E. Sand, D.R. Mason, M.A. Kirk, S.G. Roberts, K. Nordlund, S.L. Dudarev, Direct observation of size scaling and elastic interaction between nano-scale defects in collision cascades, *EPL* 110 (2015) 36001.
- [50] M. Hart, R.J. Cernik, W. Parrish, H. Toraya, Lattice-parameter determination for powders using synchrotron radiation, *J. Appl. Cryst.* 23 (1990) 286-291.
- [51] M.L. Jenkins, M.A. Kirk, *Characterization of Radiation Damage by Transmission Electron Microscopy*, First ed., IoP, Bristol & Philadelphia, 2001.
- [52] F. Francesco, T. Edmund, F. Steven, Dislocation dynamics modelling of radiation damage in thin films, *Modelling Simul. Mater. Sci. Eng.* 22 (2014) 045009.
- [53] S.L. Dudarev, P.M. Derlet, C.H. Woo, Driven mobility of self-interstitial defects under electron irradiation, *Nucl. Instrum. Methods Phys. Res. b* 256 (2007) 253-259.
- [54] Y. Matsukawa, S.J. Zinkle, One-Dimensional Fast Migration of Vacancy Clusters in Metals, *Science* 318 (2007) 959-962.
- [55] P.M. Derlet, D. Nguyen-Manh, S.L. Dudarev, Multiscale modeling of crowdion and vacancy defects in body-centered-cubic transition metals, *Phys. Rev. B* 76 (2007) 054107.
- [56] P. Hirsch, A. Howie, R. Nicholson, D.W. Pashley, M.J. Whelan, *Electron microscopy of thin crystals*, 2nd Revised ed., Krieger, Malabar, Florida, 1977.
- [57] Y.N. Osetsky, A.F. Calder, R.E. Stoller, How do energetic ions damage metallic surfaces?, *Curr. Opin. Solid State Mater. Sci.*
<http://dx.doi.org/10.1016/j.cossms.2014.1012.1001>.
- [58] W. Setyawan, G. Nandipati, K.J. Roche, H.L. Heinisch, B.D. Wirth, R.J. Kurtz, Displacement cascades and defects annealing in tungsten, Part I: Defect database from molecular dynamics simulations, *J. Nucl. Mater.* 462 (2015) 329–337.
- [59] H. Xu, R.E. Stoller, Y.N. Osetsky, D. Terentyev, Solving the Puzzle of <100> Interstitial Loop Formation in bcc Iron, *Phys. Rev. Lett.* 110 (2013) 265503.
- [60] J.P. Hirth, J. Lothe, *Theory of dislocations*, Second ed., Krieger, Malabar, Florida, 1982.
- [61] M.R. Gilbert, S.L. Dudarev, P.M. Derlet, D.G. Pettifor, Structure and metastability of mesoscopic vacancy and interstitial loop defects in iron and tungsten, *J. Phys: Condens. Matter.* 20 (2008) 345214.
- [62] B.L. Eyre, D.M. Maher, Neutron irradiation damage in molybdenum Part V. Mechanisms of vacancy and interstitial loop growth during post-irradiation annealing, *Philos. Mag.* 24 (1971) 767-797.
- [63] M.A. Kirk, I.M. Robertson, M.L. Jenkins, C.A. English, T.J. Black, J.S. Vetrano, The collapse of defect cascades to dislocation loops, *J. Nucl. Mater.* 149 (1987) 21-28.
- [64] D.E.J. Armstrong, A.J. Wilkinson, S.G. Roberts, Mechanical properties of ion-implanted tungsten–5wt% tantalum, *Phys. Scr.* T145 (2011) 014076.
- [65] X.-S. Kong, X. Wu, Y.-W. You, C.S. Liu, Q.F. Fang, J.-L. Chen, G.N. Luo, Z. Wang, First-principles calculations of transition metal–solute interactions with point defects in tungsten, *Acta Mater.* 66 (2014) 172-183.
- [66] M. Muzyk, D. Nguyen-Manh, K.J. Kurzydłowski, N.L. Baluc, S.L. Dudarev, Phase stability, point defects, and elastic properties of W-V and W-Ta alloys, *Phys. Rev. B* 84 (2011) 104115.
- [67] J.S. Hirschhorn, Stacking faults in the refractory metals and alloys - A review, *J. Less. Com. Met.* 5 (1963) 493-509.
- [68] L. Malerba, D. Terentyev, P. Olsson, R. Chakarova, J. Wallenius, Molecular dynamics simulation of displacement cascades in Fe–Cr alloys, *Journal of Nuclear Materials* 329–333, Part B (2004) 1156-1160.

- [69] M.R. Gilbert. Private communication. CCFE, 2015.
- [70] S.P. Fitzgerald, Crowdion–solute interactions: Analytical modelling and stochastic simulation, Nucl. Instrum. Methods Phys. Res. B. 352 (2015) 14-17.
- [71] J.W. Corbett, Electron radiation damage in semiconductors and metals, First ed., Academic Press, New York & London, 1966.

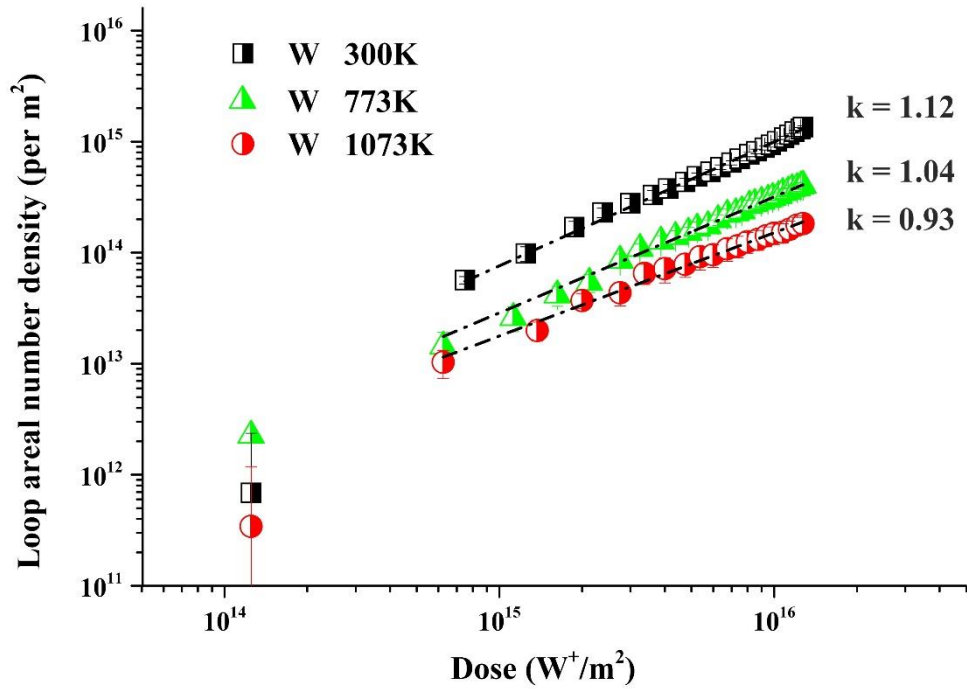


Fig. 1. Accumulation of defects as a function of dose at different irradiation temperatures during early-stage damage in pure W (≤ 0.01 dpa). The loop areal number density (loops m^{-2}) is plotted against the irradiation dose ($\text{W}^+ \text{m}^{-2}$) on a log-log scale. Each set of data is fitted by a straight line, the slope of which is assigned ‘ k ’.

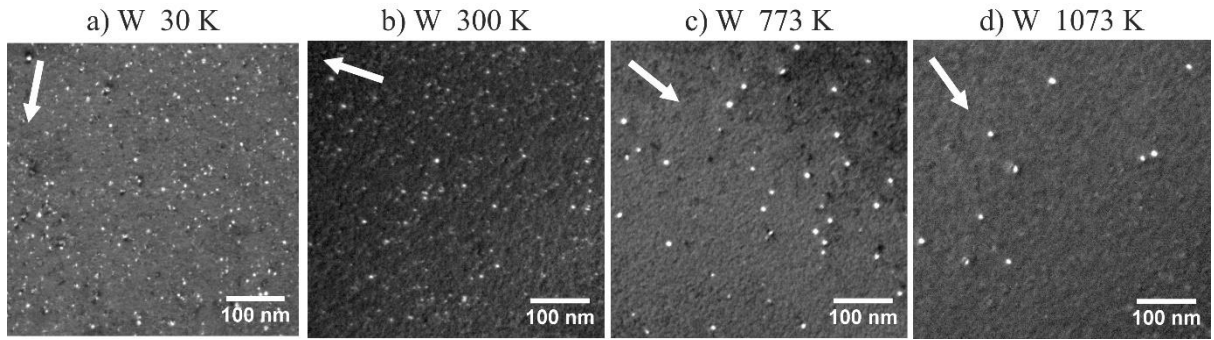


Fig. 2. Damage microstructures in pure W irradiated to 0.01 dpa, as a function of temperature from Stage I (30 K) to Stage IV (1073 K). The micrographs were recorded under weak-beam dark-field condition ($g = 200$, 3-4 g).

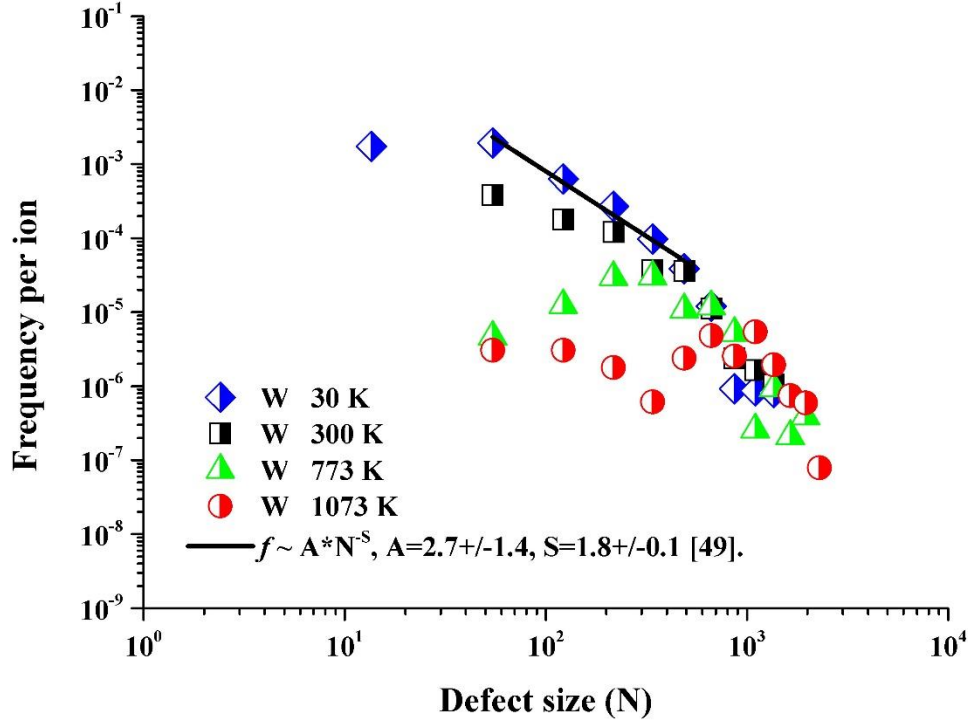


Fig. 3. The frequency of occurrence f is plotted against the cluster size N (number of point defects in the observed loops) on a log-log scale for irradiation temperatures from 30 K [49] to 1073 K, in pure W irradiated to 0.01 dpa.

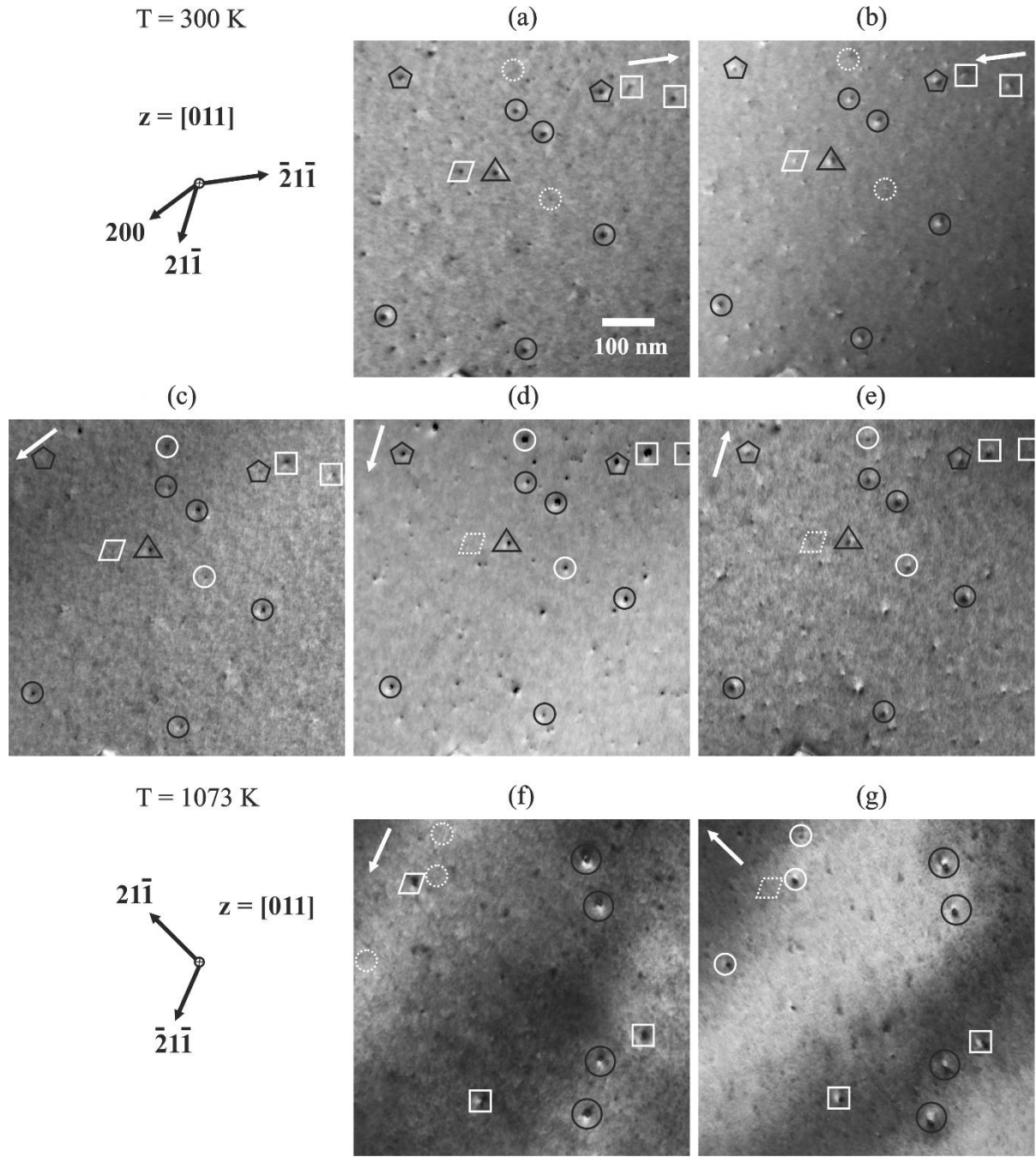


Fig. 4. Black-white contrast imaging of early-stage damage in pure W irradiated at 300 K (a-e) and 1073 K (f, g). Micrographs were recorded in dark-field, with $\mathbf{g} = 200, \pm(2\bar{1}\bar{1})$ and $\pm(21\bar{1})$ strongly excited at close to $\mathbf{z} = [011]$ orientation. Labels were introduced to distinguish different categories of loop geometry (Burgers vector, habit plane). Solid /-dashed lines represent contrast visibility / invisibility with respect to the diffraction condition.

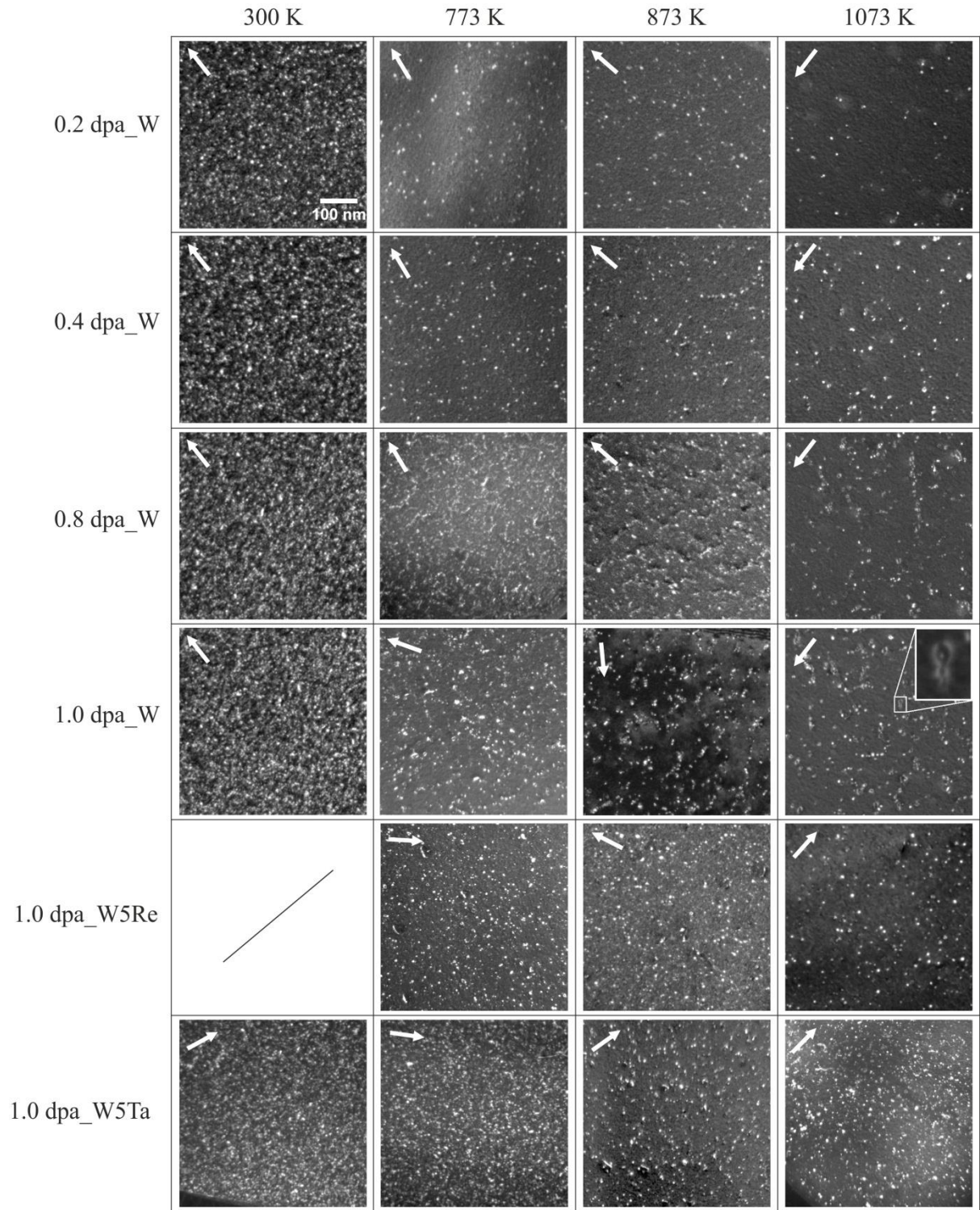


Fig. 5. Microstructural evolution in pure W and W- 5wt% (Re; Ta) alloys as a function of dose (0.2, 0.4, 0.8, 1.0 dpa) and temperature (300 - 1073 K). All micrographs shown were recorded close to $z = \langle 001 \rangle$ under weak-beam dark-field condition ($g = 200, 3-4g$). An example of finger-shaped loop has been labelled with ' \square ' in the micrograph representing pure W, irradiated at 1073 K up to 1.0 dpa; alongside which is the zoomed-in image.

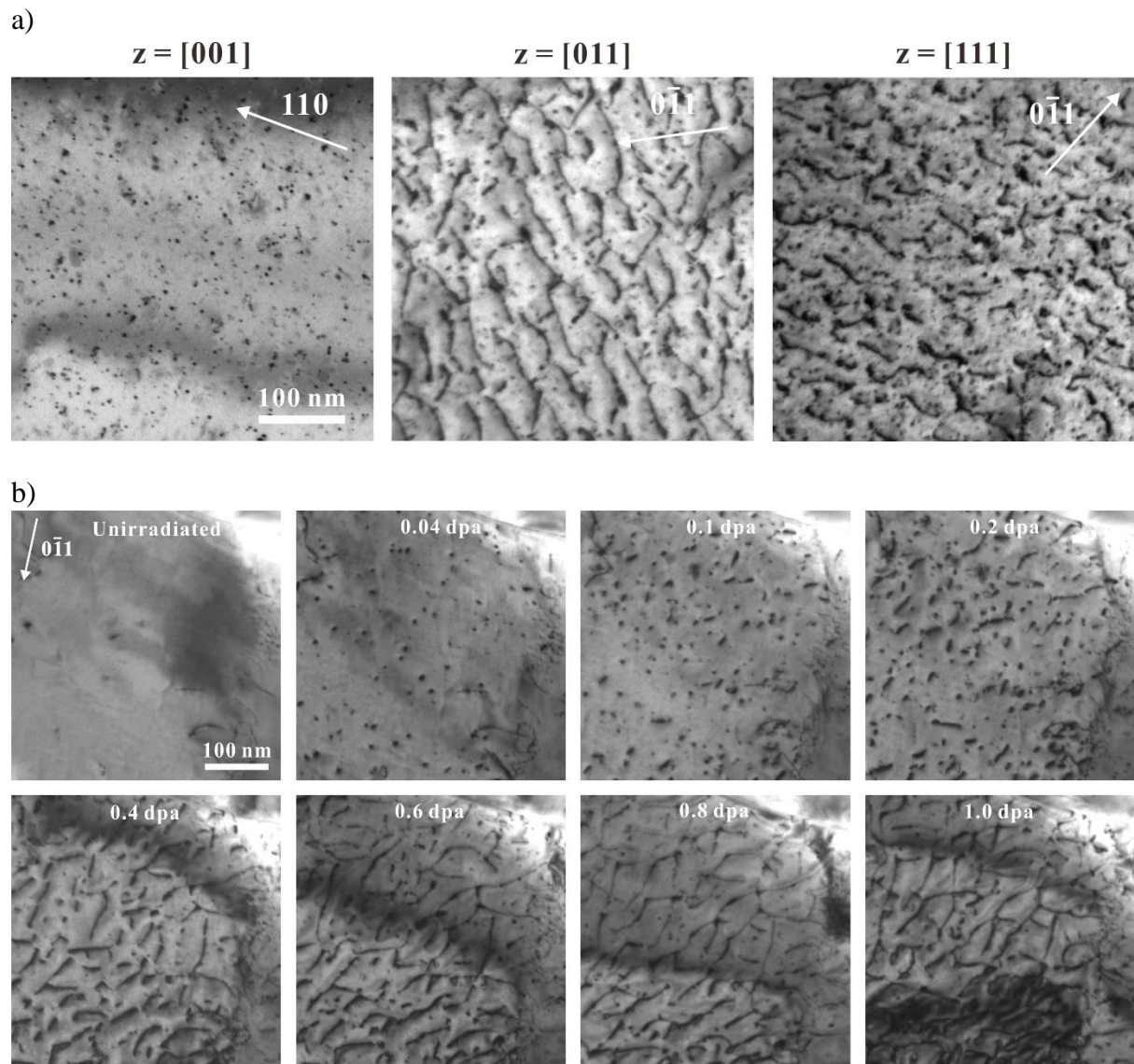


Fig. 6. The formation of loop strings and networks are favoured in non $\langle 001 \rangle$ orientations. a) Damage microstructures of W-5Ta irradiated at 773 K to 1.0 dpa are compared in $[001]$, $[011]$ and $[111]$ oriented grains; b) Snapshots of loop string and network development in W-5V, irradiated at 1073 K in $z = [011]$ orientation.

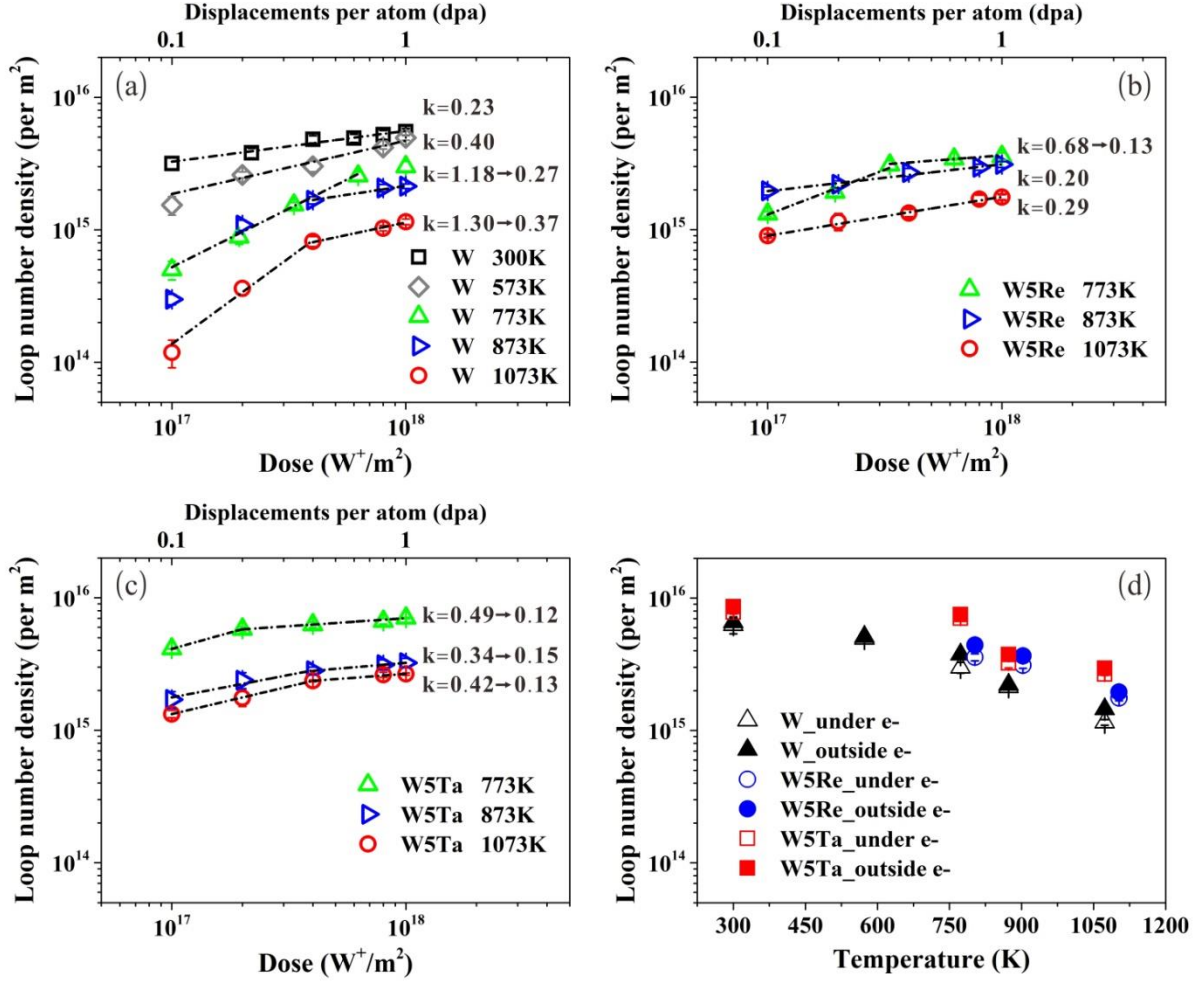


Fig. 7. The evolution of defect population in a) pure W, b) W-5Re and c) W-5Ta as a function of dose (0.1 - 1.0 dpa) and temperature (300 - 1073 K). The irradiation dose is plotted against the loop areal number density on a log-log scale. Each set of data is fitted with one or two straight lines, the slopes of which are assigned 'k'. d) An overall comparison of defect population in pure W, W-5Re and W-5Ta, based on post-irradiation characterizations (1.0 dpa; $\langle 001 \rangle$ grains) for regions under and outside the electron beam. For purpose of clarity, data points of W-5Re have been shifted by + 30 K on the temperature axis.

Fig. 8 a) is a modified version of Fig. 2 a) from Yi *et al*, 'In-situ electron microscope observations and analysis of radiation damage in tungsten', Microsc. Microanal. 21 (Suppl 3), 2015. Reproduced with permission (No. 3756100833610).

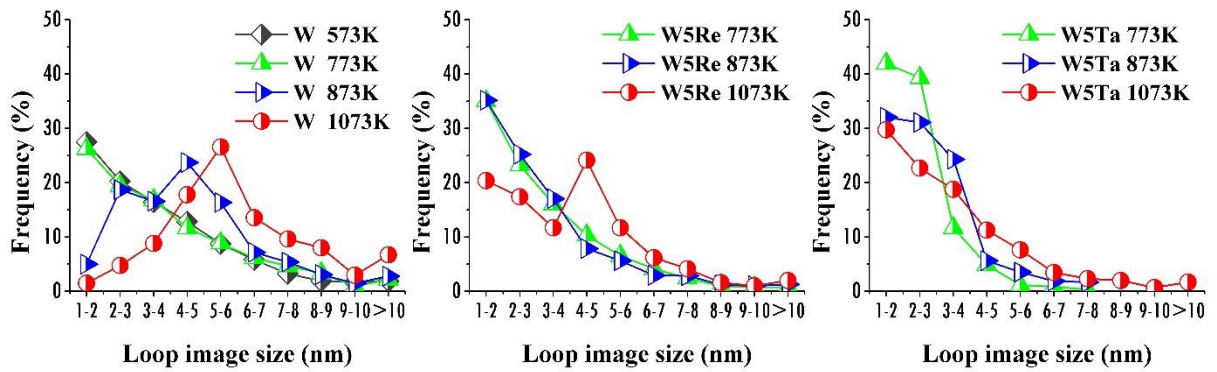


Fig. 8. Loop size distributions in pure W, W-5Re and W-5Ta irradiated to 1.0 dpa at close to $z = \langle 001 \rangle$ are plotted against the irradiation temperature.

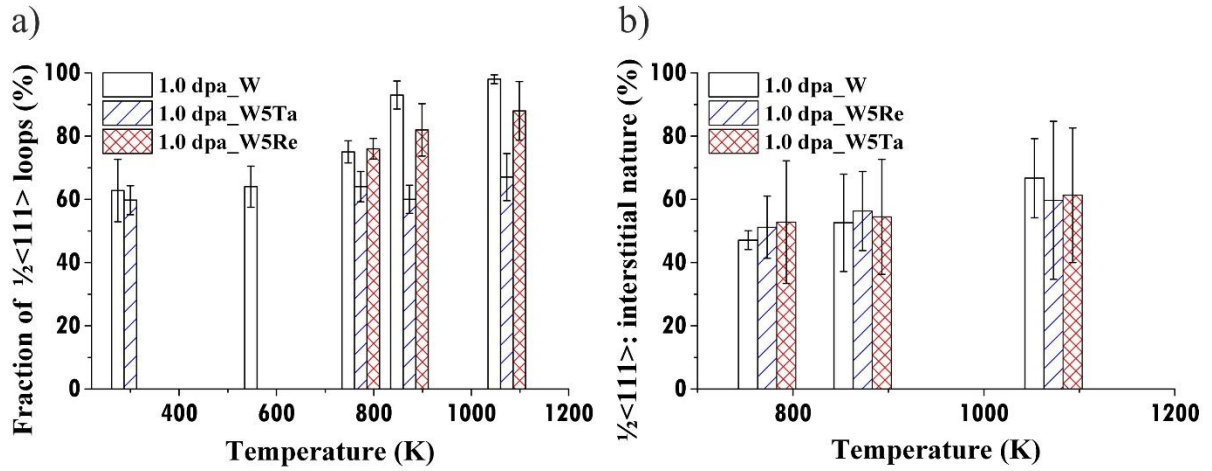


Fig. 9. a) The fractions of $\frac{1}{2} \langle 111 \rangle$ loops among overall defect populations and b) the fractions of $\frac{1}{2} \langle 111 \rangle$ loops (diameter ≥ 4 nm) which are interstitial in nature are plotted against the irradiation temperature, for pure W, W-5Re and W-5Ta irradiated to 1.0 dpa at close to $\mathbf{z} = \langle 001 \rangle$.

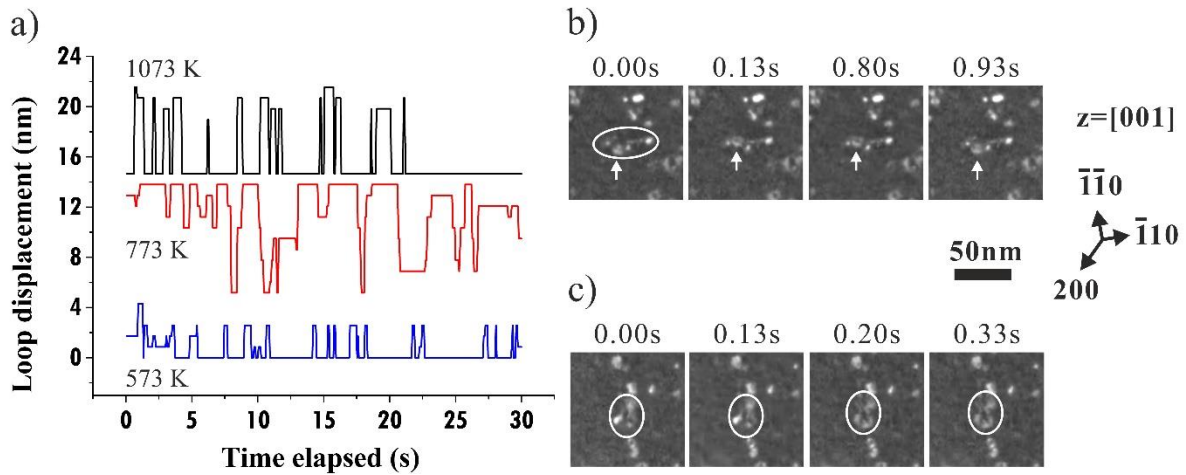


Fig. 10. Summary of dynamic behaviours of loops in pure W. a) 1D migration of $\frac{1}{2} \langle 111 \rangle$ loops as a function of temperature. Loop displacement data were extracted from 3-4 nm loops in pure W (300 K, 1.0 dpa) during post-irradiation annealing of ~ 30 min at 573 K, 773 K and 1073 K respectively. b) 1D alignment of a loop (\uparrow) with its neighbours (as circled), and c) the coalescence of loops into a 'finger-shaped' product (as circled) due to loop-loop interactions observed in pure W (1073 K, $\mathbf{z} = [001]$).

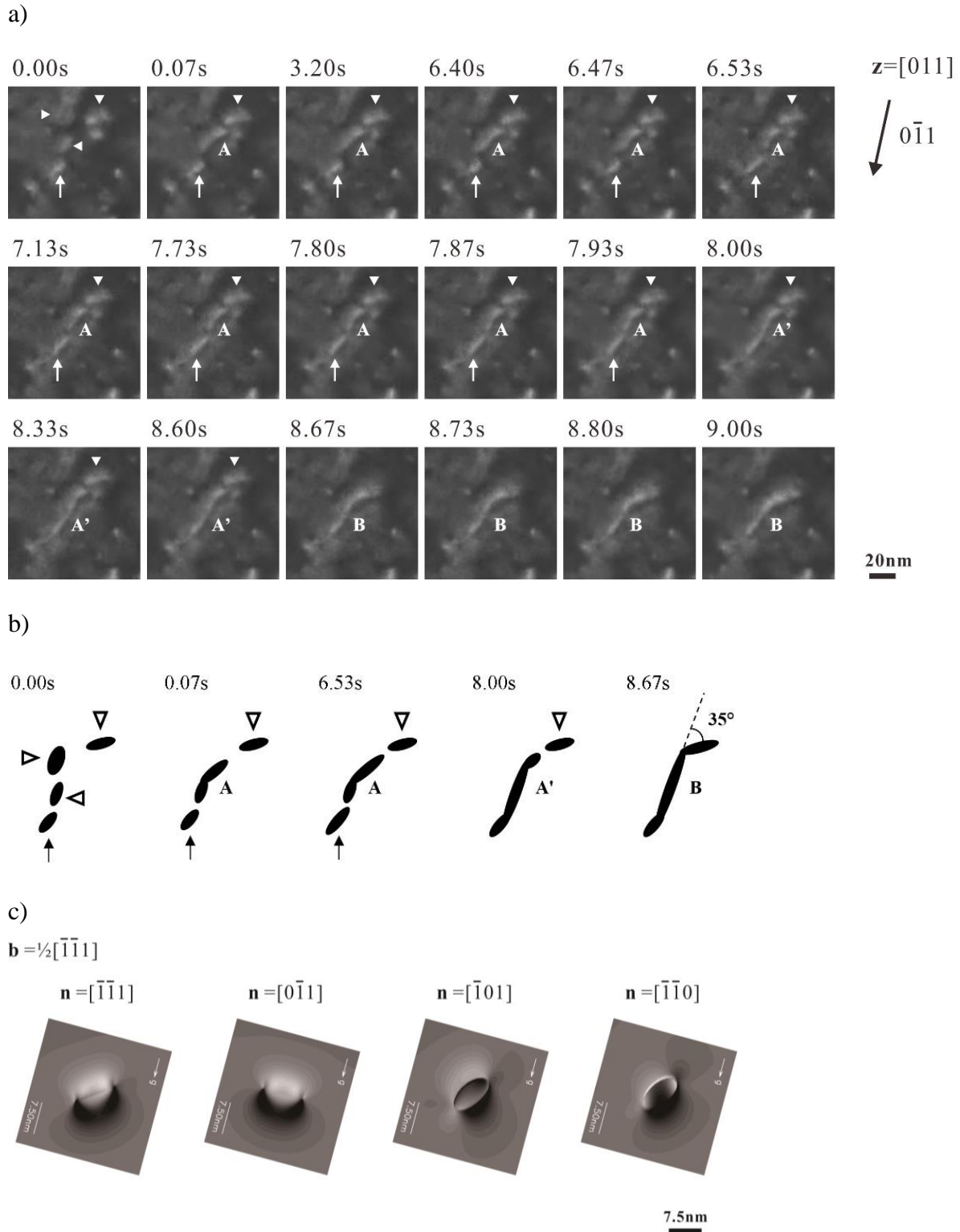


Fig. 11. Loop - loop interaction followed by coalescence into a loop configuration in W-5V, irradiated at 1073 K at close to $\mathbf{z} = [011]$ orientation. a) Frame sequences illustrating the process of loop string formation involving the interactions of loops (A; C, ‘►’; D, ‘◄’; F, ‘▼’) and strings (A', B); b) a schematic illustration of this process; c) TEMACI image simulations of a loop with $\mathbf{b} = \pm \frac{1}{2} [1\bar{1}1]$ and $\pm \frac{1}{2} [\bar{1}\bar{1}1]$ under weak-beam dark-field $\mathbf{g} = 0\bar{1}1$, $3.5\mathbf{g}$. \mathbf{n} stands for the habit plane normal. Foil thickness: 100 nm. Loop diameter: 10 nm. Depth of the loop in the foil: 15 nm. See also supplementary video 3.

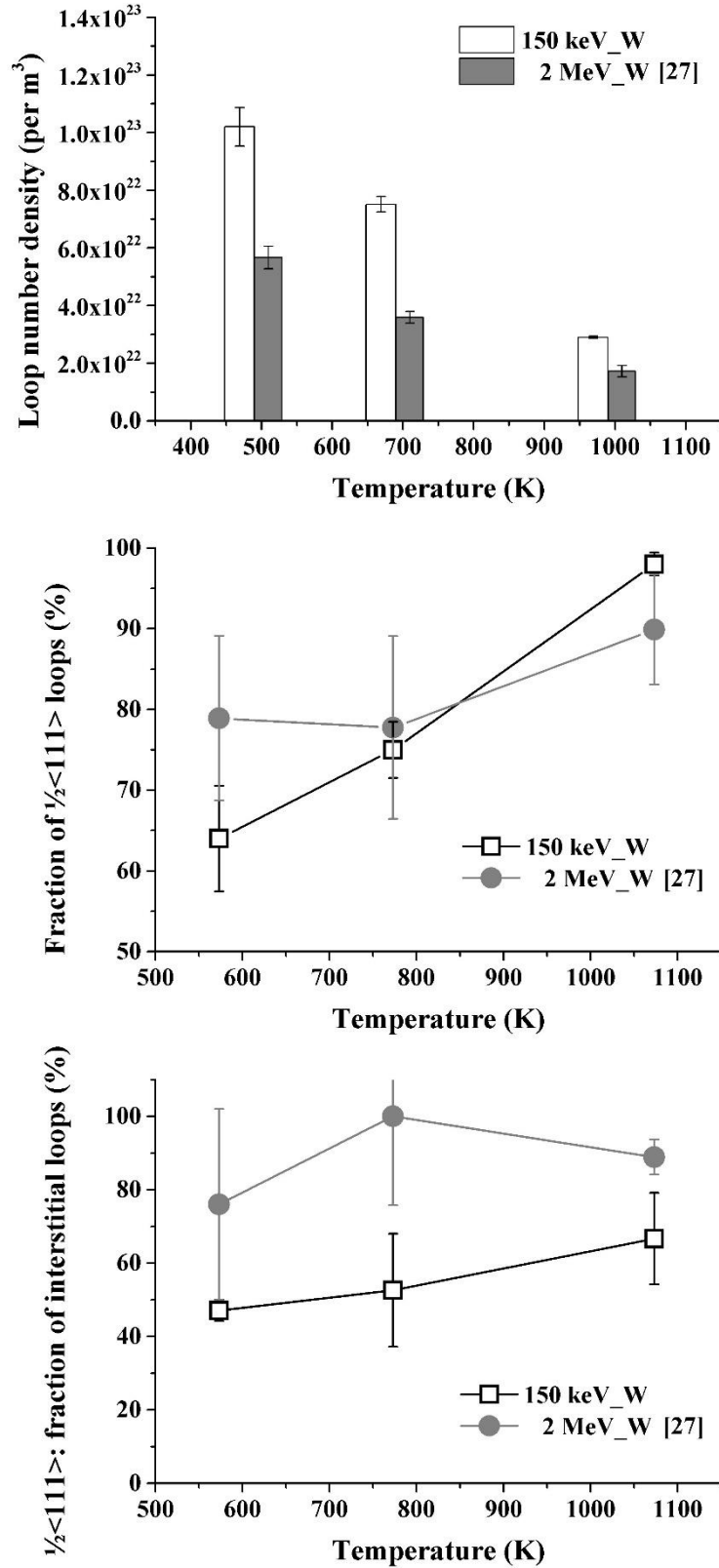
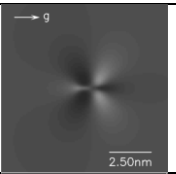
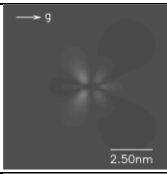
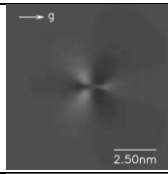
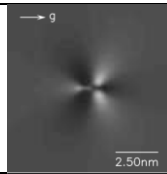
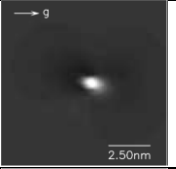
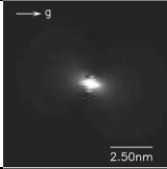
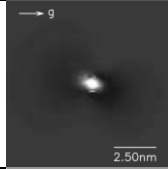
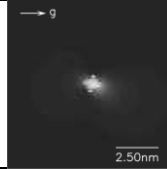
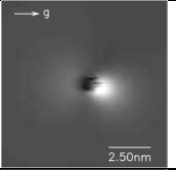
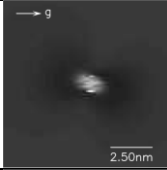
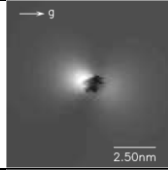
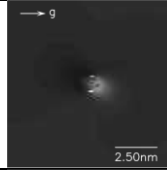
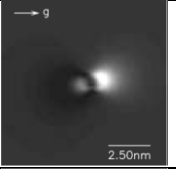
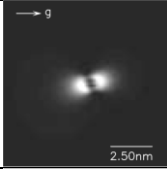
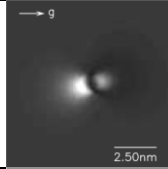
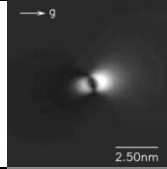
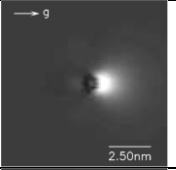
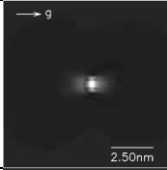
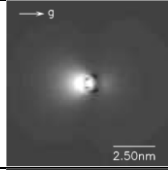
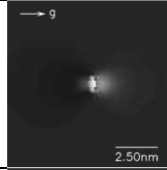
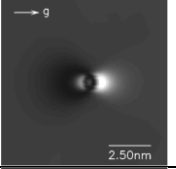
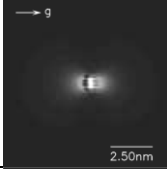
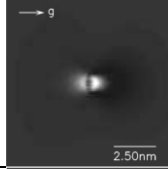
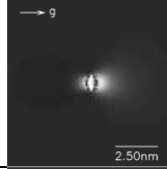
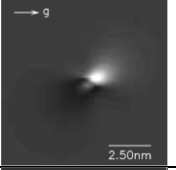
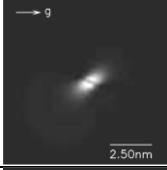
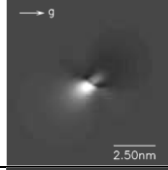
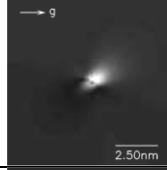
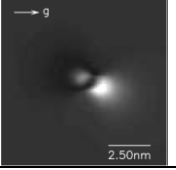
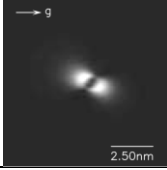
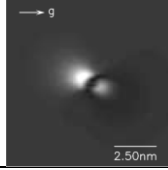
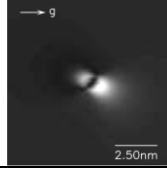


Fig. 12. Comparison between 150 keV W⁺ thin-foil [this work] and 2 MeV W⁺ near-bulk irradiations [27] of loop number densities, loop geometry (1/2 <111> versus <100> type) and loop nature (interstitial versus vacancy type) in pure W. Note that the conversion to volume density in the 150 keV W⁺ case assumed the depth range of loops to be 50 nm [12].

Depth	52 nm	56 nm	60 nm	64 nm
$\mathbf{b} = \frac{1}{2}[11\bar{1}]$ $\mathbf{n} = [11\bar{1}]$				
$\mathbf{b} = \frac{1}{2}[\bar{1}11]$ $\mathbf{n} = [\bar{1}11]$				
$\mathbf{b} = \frac{1}{2}[111]$ $\mathbf{n} = [111]$				
$\mathbf{b} = \frac{1}{2}[1\bar{1}1]$ $\mathbf{n} = [1\bar{1}1]$				
$\mathbf{b} = \frac{1}{2}[1\bar{1}\bar{1}]$ $\mathbf{n} = [101]$				
$\mathbf{b} = \frac{1}{2}[1\bar{1}\bar{1}]$ $\mathbf{n} = [1\bar{1}0]$				
$\mathbf{b} = \frac{1}{2}[1\bar{1}\bar{1}]$ $\mathbf{n} = [0\bar{1}1]$				
$\mathbf{b} = [100]$ $\mathbf{n} = [100]$				

Supplementary figure. Image simulations (TEMACI code) were performed on the black-white contrasts of vacancy loops in tungsten, in order for comparison with the experimental data shown in Fig. 4. The simulations were for a $\mathbf{b} = [100]$ loop and four variants of $\mathbf{b} = \frac{1}{2}\langle 111 \rangle$ loops in a foil of 66 nm with $\mathbf{z} = [011]$. Loop depth 52 - 64 nm; loop diameter 1 nm; loop normal \mathbf{n} ; diffraction condition $\mathbf{g} = \bar{2}1\bar{1}$.